



# Advanced nanostructured photocatalysts based on reduced graphene oxide–TiO<sub>2</sub> composites for degradation of diphenhydramine pharmaceutical and methyl orange dye

Luisa M. Pastrana-Martínez<sup>a</sup>, Sergio Morales-Torres<sup>a</sup>, Vlassis Likodimos<sup>b</sup>, José L. Figueiredo<sup>a</sup>, Joaquim L. Faria<sup>a</sup>, Polycarpos Falaras<sup>b,\*\*</sup>, Adrián M.T. Silva<sup>a,\*</sup>

<sup>a</sup> LCM – Laboratory of Catalysis and Materials – Associate Laboratory LSRE/LCM, Faculdade de Engenharia, Universidade do Porto, Rua Dr. Roberto Frias, 4200-465 Porto, Portugal

<sup>b</sup> Institute of Physical Chemistry, NCSR Demokritos, 15310 Aghia Paraskevi, Attikis, Athens, Greece

## ARTICLE INFO

### Article history:

Received 25 January 2012

Received in revised form 26 April 2012

Accepted 27 April 2012

Available online 6 May 2012

### Keywords:

Reduced graphene oxide

Titanium dioxide

Heterogeneous photocatalysis

Scavengers for holes and radicals

Photoluminescence quenching

Raman spectroscopy

## ABSTRACT

Reduced graphene oxide–TiO<sub>2</sub> composites (GOT) were prepared by liquid phase deposition followed by post-thermal reduction at different temperatures. The composite materials were systematically evaluated as photocatalysts for the degradation of an important pharmaceutical water pollutant, diphenhydramine (DP), and an azo-dye, methyl orange (MO), under both near-UV/Vis and visible light irradiation as a function of the graphene oxide (GO) content. A marked compositional dependence of the photocatalytic activity was evidenced for DP and MO pollutants degradation and mineralization under both UV/Vis and visible light. Especially under visible light, optimum photocatalytic performance was obtained for the composites treated at 200 °C comprising 3.3–4.0 wt.% GO, exceeding that of the benchmark P25 (Evonik) catalyst. According to scanning electron microscopy, Raman spectroscopy, and porosimetry analysis data, this was attributed to the optimal assembly and interfacial coupling between the reduced GO sheets and TiO<sub>2</sub> nanoparticles. Almost total degradation and significant mineralization of DP and MO pollutants (in less than 60 min) was achieved under near-UV/Vis irradiation for the optimum GOT composites. However, higher GO content and calcination temperatures (350 °C) led to detrimental effects due to the GO excess and the disruption of the GO–TiO<sub>2</sub> binding. Photocatalytic experiments employing sacrificial hole and radical scavenging agents revealed that photogenerated holes are the primary active species in DP degradation for both bare TiO<sub>2</sub> and GOT under UV/Vis irradiation, while an enhanced contribution of radical mediated DP oxidation was evidenced under visible light. These results combined with the distinct quenching of the GO photoluminescence under visible and NIR laser excitation, indicate that reduced GO acts either as electron acceptor or electron donor (sensitizer) of TiO<sub>2</sub> under UV and visible light, respectively. Fine-tuning of the reduced GO–TiO<sub>2</sub> interface is concluded as a very promising route to alleviate electron–hole recombination and circumvent the inherently poor light harvesting ability of TiO<sub>2</sub> in the visible range.

© 2012 Elsevier B.V. All rights reserved.

## 1. Introduction

Graphene, the two dimensional carbon allotrope consisting of a single atomic layer honeycomb network of sp<sup>2</sup>-hybridization, was experimentally sought long before [1] its pioneering isolation and identification in 2004 [2] that rendered it as one of the most exciting and challenging materials for both fundamental science and future technological applications. The unique electronic,

optical, mechanical, and thermal properties of graphene [3,4] has stimulated immense interest for the design of novel graphene based functional materials that could be integrated in diverse applications, ranging from nanoelectronics [5,6], biosensing [7] and hydrogen storage [8], to supercapacitor electrodes [9–11], catalysis [12] and more recently heterogeneous photocatalysis [13].

Titanium dioxide (TiO<sub>2</sub>) photocatalysis has emerged as a highly promising advanced oxidation technology that could decisively contribute in the abatement of environmental pollution based on the utilization of solar energy [14–20]. Ample verification of the effectiveness of TiO<sub>2</sub> to generate highly reactive chemical species such as hydroxyl radicals, upon UV light illumination along with its environmentally benign properties (i.e., non-toxicity, absence of dissolution in water, photostability) and relatively low cost,

\* Corresponding author. Tel.: +351 22 5081582; fax: +351 22 5081449.

\*\* Corresponding author. Tel.: +30 210 6503644; fax: +30 210 6511766.

E-mail addresses: [papi@chem.demokritos.gr](mailto:papi@chem.demokritos.gr) (P. Falaras), [adrian@fe.up.pt](mailto:adrian@fe.up.pt) (A.M.T. Silva).

rendered  $\text{TiO}_2$  a key material for the complete destruction of hazardous organic pollutants in water and air [21,22].

However, practical application of  $\text{TiO}_2$  photocatalytic materials is severely compromised by two inherent limitations, namely the low quantum yield, which is primarily impaired by the recombination of photo-generated charge carriers, and the poor light-harvesting ability that is restricted by the wide band gap of  $\text{TiO}_2$  to the UVA spectral range [21,23]. A highly appealing approach toward the development of nanocomposite photocatalysts relies on the combination of  $\text{TiO}_2$  with carbonaceous materials including mesoporous carbon and carbon nanotubes [24–26], and more recently graphene based materials, the substrate of choice being graphene oxide (GO) [13].

Graphene oxide offers exciting opportunities for next generation photocatalysts as GO can be readily prepared by the exfoliation of graphite oxide [27,28] providing a two dimensional substrate decorated by oxygen functional groups on the basal planes and the layer edges affording abundant reactive and anchoring sites for the assembly of graphene based nanocomposite materials [29]. Besides its rich surface chemistry, GO exhibits a highly heterogeneous electronic structure determined by the interplay of conducting  $\pi$ -states from  $\text{sp}^2$  carbon atoms within the large energy gap ( $\sigma$ -states) of the  $\text{sp}^3$  matrix [30]. The challenging control of the ratio between the  $\text{sp}^2$  and  $\text{sp}^3$  fractions by means of chemical and/or thermal reduction may radically modify the GO electronic properties from the insulating up to the graphene-like semi-metallic state under optimal processing conditions. Most importantly, significant enhancement of the photocatalytic activity has been frequently observed when GO is combined with  $\text{TiO}_2$ , due to their synergetic interaction encompassing both interfacial electron transfer between the two constituent phases and the markedly enhanced adsorption capacity of GO for pollutant molecules [13]. In particular, Kamat and co-workers [31,32] have demonstrated that photo-generated electrons in  $\text{TiO}_2$  upon UV irradiation are transferred and subsequently transported across the GO sheets, leading to their reduction and providing an efficient means of charge separation on the composite photocatalyst under UV irradiation. This seminal work has spawned widespread research efforts on the development of efficient GO– $\text{TiO}_2$  composite photocatalysts employing different synthetic routes that could exploit GO as highly adsorptive substrate acting simultaneously as a scavenger and shuttle of electrons for the enhancement of the  $\text{TiO}_2$  photocatalytic performance [33–48].

However, despite the rapid progress in the development of graphene based  $\text{TiO}_2$  composites, optimization of the GO– $\text{TiO}_2$  interface and the accompanying electron transfer remains a major challenge that critically affects the materials photocatalytic performance [34,40,42]. Moreover, evaluation of the composites' photocatalytic efficiency has been mainly limited to the degradation of dye pollutants [13,49], the most notable exceptions being their recent application for the photocatalytic degradation of volatile organic pollutants in the gas phase [41] and the photo-reductive conversion of Cr(VI) [34]. Furthermore, a key prospect of graphene based  $\text{TiO}_2$  photocatalysts is their activation by visible light [13], the underlying mechanism of which remains essentially unexplored [48]. In fact, most photocatalytic experiments have been performed using dyes as model organic pollutants, which are prone to self-sensitized photocatalytic degradation upon absorption of visible light [50], and thus may effectively obscure the reaction mechanism of graphene based  $\text{TiO}_2$  photocatalysts under visible light. Based on the expected energetics for an ideal graphene/ $\text{TiO}_2$  heterojunction and the verified acceptor action of graphene, it has been proposed that the photocatalytic activity of graphene based  $\text{TiO}_2$  composites under visible light is due to the dye self-sensitized photocatalytic mechanism [47]. In that case,

electron transfer would take place from the visible light photo-excited dye molecules to the semiconductor conduction band and then to graphene that serves as an electron scavenger similar to its action under UV irradiation. However, this interpretation is challenged by recent photocurrent measurements and theoretical predictions suggesting that graphene or GO may also act as an electron donor to  $\text{TiO}_2$  under visible light [38,51], which upon firm experimental verification can be of high value for the enhancement of solar harvesting by  $\text{TiO}_2$ .

The aim of the present work relies on the investigation and optimization of the assembly and interfacial coupling of  $\text{TiO}_2$  nanoparticles on graphene oxide sheets, exploiting the *in situ* liquid phase deposition followed by thermal reduction in  $\text{N}_2$  atmosphere. The work is particularly aimed at establishing firm structure-activity relationships and providing solid data on the photocatalytic performance of reduced graphene oxide– $\text{TiO}_2$  (GOT) composites, as well as exploring their potential as efficient visible light activated photocatalysts. To this end, the photocatalytic activity of the GOT photocatalysts was systematically evaluated as a function of the GO content and thermal treatment temperature for the degradation and mineralization of a hazardous colourless pharmaceutical, diphenhydramine (DP), recently first reported by us in what concerns heterogeneous photocatalytic degradation [52], and a well-known organic dye, methyl orange (MO) under both near-UV/Vis and visible light irradiation. Both pollutants are found in industrial waters and waste waters and present low biodegradability [53,54], while their different absorption characteristics (UV and Vis range) offer the possibility to address the visible light photocatalytic mechanism. In fact, the pronounced quenching of the GO photoluminescence under visible laser excitation, together with the enhanced radical mediated oxidation evidenced by hole and radical trapping experiments, revealed that reduced GO can operate as a visible light sensitizer of  $\text{TiO}_2$ , a key issue in  $\text{TiO}_2$  photocatalysis that has been marginally addressed for GO– $\text{TiO}_2$  composites. Thereby, it is suggested that reduced GO– $\text{TiO}_2$  heterostructures may enable the photocatalytic action of  $\text{TiO}_2$  in the visible range without compromising its activity under UV irradiation, a major drawback of most visible light active anion doped  $\text{TiO}_2$  photocatalysts.

## 2. Experimental

### 2.1. Synthesis of graphene oxide

The modified Hummers method [28,55] was used to oxidize natural graphite (20  $\mu\text{m}$ , Sigma-Aldrich). In a typical procedure, 50 mL of  $\text{H}_2\text{SO}_4$  was added gradually with stirring and cooling to a 500 mL flask containing 2 g of graphite. Then 6 g of potassium permanganate ( $\text{KMnO}_4$ ) was added slowly to the mixture. The suspension was continuously stirred for 2 h at 35 °C. After that, it was cooled in an ice bath and subsequently diluted by 350 mL of deionized water. Then  $\text{H}_2\text{O}_2$  (30%, w/v) was added in order to reduce residual permanganate to soluble manganese ions, appearing a bright yellow colour in the suspension. The oxidized material was purified with a 10% HCl solution and then the suspension was filtered, washed several times with water until achieve a neutral pH in the resulting water, and dried at 60 °C for 24 h to obtain graphite oxide. The resulting material was dispersed in a given volume of water and sonicated in an ultrasound bath (ultrasonic processor UP400S, 24 kHz) for 1 h. The sonicated dispersion was centrifuged for 20 min at 3000 rpm to remove unexfoliated graphite oxide particles from the supernatant and the obtained suspension of graphene oxide was then used for the synthesis of GOT composites.

## 2.2. Preparation of reduced graphene oxide– $\text{TiO}_2$ composites (GOT)

GOT composites were synthesized by using the liquid phase deposition method (LPD) at room temperature as described elsewhere [34,39]. Different amounts of the graphene oxide dispersion ( $0.5 \text{ g L}^{-1}$ ) were diluted with distilled water (250 mL) in order to obtain composites with different graphene oxide contents. In each run, ammonium hexafluorotitanate (IV),  $(\text{NH}_4)_2\text{TiF}_6$  ( $0.1 \text{ mol L}^{-1}$ ), and boric acid,  $\text{H}_3\text{BO}_3$  ( $0.3 \text{ mol L}^{-1}$ ), were added to the dispersion heated in an oil bath ( $60^\circ\text{C}$  for 2 h) under vigorous stirring with the aim to obtain a homogeneous suspension. The precipitate was separated by filtration, washed with water and dried at  $100^\circ\text{C}$  under vacuum for 2 h. The obtained solid was treated in a furnace with  $\text{N}_2$  flow at  $5^\circ\text{C min}^{-1}$  until the desired temperature ( $200^\circ\text{C}$  or  $350^\circ\text{C}$ ) and with soak time of 3 h.

During thermal treatments of GOT composites, it is known that the partial reduction of graphene oxide occurs with simultaneous deposition of  $\text{TiO}_2$  onto the reduced graphene oxide [35] and exclusively anatase  $\text{TiO}_2$  particles are formed at such temperatures regardless of the graphene oxide content [34]. The GOT composites will be denoted as GOT-X-Y, where X and Y refers to the graphene oxide content (1.2 wt.%, 3.3 wt.%, 4.0 wt.%, 5.4 wt.%, 8.0 wt.% or 12.0 wt.%) and temperature treatment ( $200^\circ\text{C}$  and  $350^\circ\text{C}$ ), respectively. For instance, GOT-3.3-200 refers to the composite prepared with 3.3 wt.% of graphene oxide and treated at  $200^\circ\text{C}$ . The composites that were not submitted to the thermal treatment are referred as GOT-X-nt. Bare  $\text{TiO}_2$  was also prepared by using the same method but without addition of graphene oxide ( $\text{TiO}_2$ -nt) and treated at  $200^\circ\text{C}$  ( $\text{TiO}_2$ -200). Degussa P25 from Evonik was used as reference material.

## 2.3. Materials characterization

Atomic force microscopy (AFM) was performed on a Veeco Metrology Nanoscope IVA atomic force microscope, operating in tapping mode. For the AFM imaging, a graphene oxide dilute aqueous dispersion (1:40) was dropped onto fresh glass substrate and dried in air at room temperature. Thermogravimetric (TG) and differential thermogravimetric (DTG) analyses of the GOT composites were performed by heating the sample in air flow from  $50^\circ\text{C}$  to  $1000^\circ\text{C}$  at  $20^\circ\text{C min}^{-1}$  using a STA 490 PC/4/H Luxx Netzsch thermal analyser; the graphene oxide content (wt.%) in a given composite was estimated by subtracting the weight loss of  $\text{TiO}_2$ -nt to the weight loss obtained with the composite.

Textural characterization of the samples was carried out by  $\text{N}_2$  adsorption–desorption at  $-196^\circ\text{C}$  with a Quantachrome NOVA 4200e apparatus. The Brunauer–Emmett–Teller (BET) [56] and Dubinin–Radushkevich [57] equations were applied to determine the apparent surface area ( $S_{\text{BET}}$ ) and the micropore volume ( $V_{\text{micro}}$ ), respectively. The BJH method [58] was applied to the desorption branch of the  $\text{N}_2$  isotherms to obtain the volume ( $V_{\text{meso}}$ ) and cumulative surface area ( $S_{\text{BJH}}$ ) of the mesopores. The morphology of the composites was determined by scanning electron microscopy (SEM) FEI Quanta 400FEG ESEM/EDAX Genesis X4M instrument. High resolution electron microscopy (HRTEM) observations were performed on a JEOL JEM-2100, operating at 200 kV.

XPS measurements of selected samples were made with a VG Scientific ESCALAB 200A spectrometer equipped with a non-monochromatized  $\text{AlK}\alpha$  radiation ( $h\nu = 1486.6 \text{ eV}$ ). For these measurements, the binding energy (BE) values were referred to the C1s peak at 284.9 eV. Survey and multi-region spectra were recorded at C1s, O1s, F1s and Ti2p photoelectron peaks. Each spectral region of photoelectron interest was scanned several times to obtain good signal-to-noise ratios. The spectra obtained after

a Shirley background subtraction were fitted to Lorentzian and Gaussian curves using XPS peak 4.1 software.

The optical properties of the samples were analyzed by UV/Vis diffuse reflectance spectroscopy using a JASCO V-560 UV/Vis spectrophotometer, equipped with an integrating sphere attachment (JASCO ISV-469). Barium sulfate ( $\text{BaSO}_4$ ) was used as a reference. The reflectance spectra were converted by the instrument software (JASCO) to equivalent absorption Kubelka–Munk units. The band gap was determined by plotting the transformed Kubelka–Munk as a function of the energy of light.

Micro-Raman spectra were measured in backscattering configuration on a Renishaw inVia Reflex microscope using an  $\text{Ar}^+$  ion laser ( $\lambda = 514.5 \text{ nm}$ ) and a high power near infrared (NIR) diode laser ( $\lambda = 785 \text{ nm}$ ) as excitation sources. The laser beam was focused onto the samples by means of a  $20\times$  objective, while the laser power density was kept below  $0.03 \text{ mW } \mu\text{m}^{-2}$  to avoid local heating. A large number of spectra were acquired from different spots for each studied sample, while the frequency shifts were calibrated by an internal Si reference. In the case of GO, measurements were carried out by casting a drop of a dilute GO dispersion on a cleaned Si wafer. Spectral deconvolution was carried out by non-linear least square fitting of the Raman peaks by Lorentzian lineshapes.

## 2.4. Photocatalytic experiments

The photocatalytic activity of the prepared composites was evaluated for the degradation of diphenhydramine, DP (Sigma–Aldrich, 99%), and methyl orange, MO (Fluka, 99%), in aqueous solutions under near-UV/Vis and visible light irradiation at room temperature (average  $25^\circ\text{C}$ ). The experiments were performed in a quartz cylindrical reactor filled with 7.5 mL of solution containing the model pollutant DP ( $3.40 \times 10^{-4} \text{ mol L}^{-1}$ ) or MO ( $3.05 \times 10^{-5} \text{ mol L}^{-1}$ ). A Heraeus TQ 150 medium-pressure mercury vapor lamp was inserted in a DURAN® glass water cooling jacket (with the aim to control the operating temperature) delivering near-UV/Vis irradiation ( $\lambda > 350 \text{ nm}$ ), irradiance being approximately  $50 \text{ mW cm}^{-2}$ . For visible light experiments a cut-off long pass filter was used ( $\lambda > 430 \text{ nm}$ ), and in this case the photon flow entering the reactor was ca.  $6 \text{ mW cm}^{-2}$ . An oxygen flow was continuously supplied to the reactor. Samples were taken from the reactor and centrifuged to separate the catalyst particles before analysis.

The optimal load of catalyst was established in preliminary photocatalytic experiments with the aim to avoid the ineffective excess of catalyst: the amount of catalysts was kept at the optimal value of  $1.0 \text{ g L}^{-1}$  and  $0.5 \text{ g L}^{-1}$  for DP and MO, respectively. Preliminary dark experiments without irradiation were also performed to establish the period of time needed to achieve the adsorption–desorption equilibrium of all the prepared materials and to determine  $t=0$  for the photocatalytic reactions (instant to turn on the irradiation). Direct photolysis in the absence of catalyst was also performed as blank experiment in order to calculate the contribution from direct photolysis.

The concentration of DP was determined by HPLC with a Hitachi Elite LaChrom system equipped with a Hydrosphere C18 column ( $250 \text{ mm} \times 4.6 \text{ mm}$ ;  $5 \mu\text{m}$  particles), a Diode Array Detector (L-2450) and a solvent delivery pump (L-2130). An isocratic method set at a flow rate of  $1 \text{ mL min}^{-1}$  was used with the eluent consisting of an A:B (70:30) mixture of  $20 \text{ mM NaH}_2\text{PO}_4$  acidified with  $\text{H}_3\text{PO}_4$  at  $\text{pH} = 2.80$  (A) and acetonitrile (B). Absorbance was found to be linear over the whole range considered. The concentration of MO was determined by UV–Vis spectrophotometry at  $464 \text{ nm}$  ( $\epsilon_{464\text{nm}} = 22068 \text{ M}^{-1} \text{ cm}^{-1}$ ) in a Jasco V-560 spectrophotometer. The total organic carbon (TOC) was also determined for selected samples using a Shimadzu TOC-5000A analyzer.

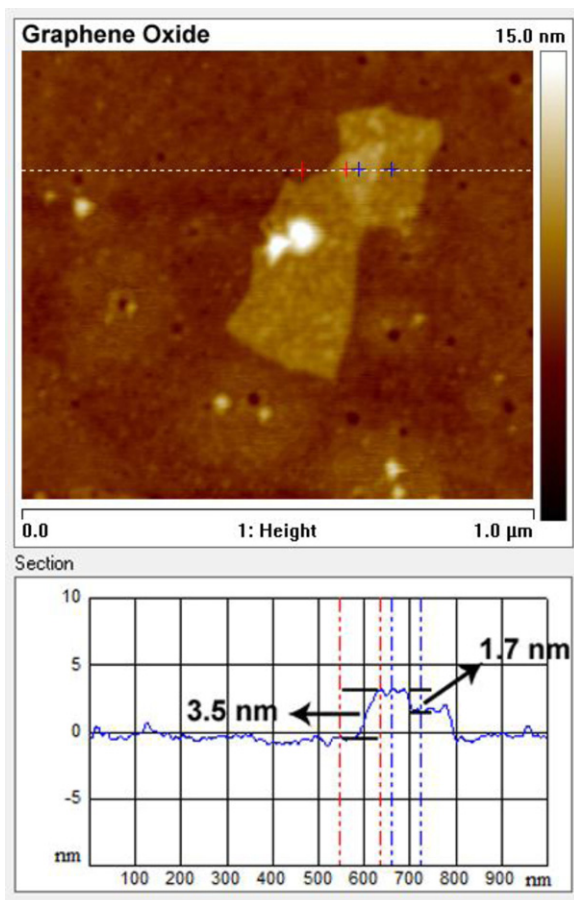


**Fig. 1.** Tapping-mode AFM image of graphene oxide and corresponding height profiles.

The experiments revealed that the photocatalytic oxidation of pollutants can be ascribed to a pseudo-first order kinetic model, as described by the following equation:

$$C = C_0 e^{-kt} \quad (1)$$

where  $C$  corresponds to pollutant concentration,  $k$  is the pseudo-first order kinetic constant,  $t$  is the reaction time and  $C_0$  is the pollutant concentration for  $t=0$ . The values of  $k$  were obtained by non-linear regression.

### 3. Results and discussion

#### 3.1. Materials characterization

##### 3.1.1. Atomic force microscopy (AFM)

AFM was applied as a suitable technique to analyse the exfoliation of graphene and its derivatives when dispersed in a solvent. Fig. 1 shows the representative results of the AFM images for samples prepared from graphene oxide dispersion in water. The images revealed the presence of two sheets of graphene oxide with a height of approximately 1.7 nm each (3.5 nm in the region where the two sheets overlap). This thickness is higher than the commonly ascribed to single-layer graphene oxide with functional groups on both sides of the sheet ( $\sim 1$  nm) [59,60], but is consistent with the reported values found in literature for exfoliated graphene oxide (i.e., 1.0 to 1.7 nm) [61,62]. This variability from 1.0 to 1.7 nm for graphene oxide could be partially attributed to uncompensated electrostatic forces in AFM analysis and also might be assigned to a layer of hydrated graphene oxide. Li et al. [27] showed that the surface charges on graphene oxide are highly negative when dispersed in

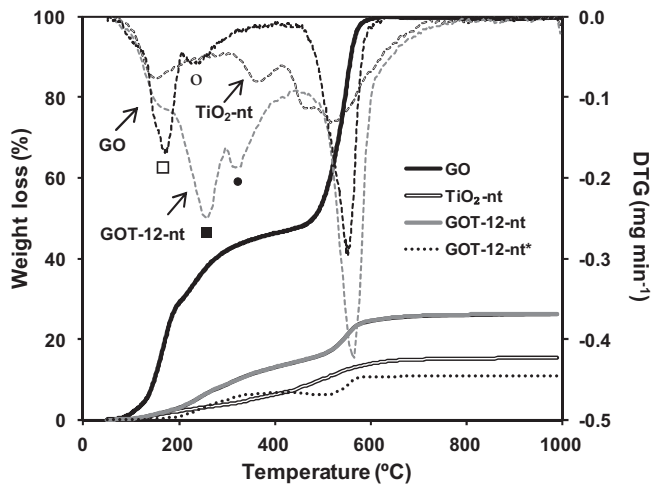


**Fig. 2.** Thermogravimetric analysis of graphene oxide,  $\text{TiO}_2\text{-nt}$  and GOT-12.0-nt. Solid and dashed lines correspond to weight loss and DTG curves, respectively. GOT-12.0-nt\* correspond to the calculated TG curve of GOT-12-nt subtracting the weight loss of  $\text{TiO}_2\text{-nt}$ . DTG peaks: graphene oxide (open symbols) and GOT-12-nt (closed symbols).

water (by measuring the zeta potential due to the ionization of the carboxylic acid and the phenolic hydroxyl groups) and, therefore, the formation of a stable graphene oxide dispersion in water should be attributed to electrostatic repulsions.

#### 3.1.2. Thermogravimetric (TG) and differential thermogravimetric (DTG) analysis

Fig. 2 shows the TG/DTG curves obtained in air atmosphere for graphene oxide,  $\text{TiO}_2\text{-nt}$  and GOT-12.0-nt. The reference GOT-12.0-nt\* corresponds to the TG curve of GOT-12-nt minus the weight loss of  $\text{TiO}_2\text{-nt}$ . Graphene oxide showed two different marked steps of weight loss: the removal of labile oxygenated surface groups ca. 150 and 250 °C, corresponding to the release of  $\text{CO}_x$  and  $\text{H}_2\text{O}$  [60,63], and a sharp mass loss around 550 °C corresponding to carbon combustion. In general, TG curves for the GOT composites begin to increase at higher temperatures than for single graphene oxide, as observed in Fig. 2 for the particular case of GOT-12.0-nt. Moreover, the weight loss curves for the GOT composites and  $\text{TiO}_2$  were similar up to ca. 200 °C, while higher weight losses were observed for the GOT composites, in comparison to  $\text{TiO}_2$ , at higher temperatures (as better exemplified in Fig. 2 by the calculated TG curve referred as GOT-12.0-nt\* = GOT-12.0-nt-TiO₂-nt). Regarding the DTG results, the profile obtained for GOT-12-nt showed two clear peaks below 400 °C, namely at 248 and 307 °C (closed symbols). Similar peaks seem to appear in the DTG curve of single graphene oxide, but at much lower temperatures (162 and 237 °C, open symbols). Therefore, these peaks seem to be shifted from lower to higher temperatures in the presence of  $\text{TiO}_2$ . These results suggest that the oxygenated surface groups of the graphene oxide could interact with the deposited  $\text{TiO}_2$  particles [34] leading to the stabilization of these oxygenated groups. In addition, at temperatures near to 550 °C (548 and 556 °C for graphene oxide and GOT-12-nt, respectively), both samples show a sharp peak corresponding to carbon combustion, which was already noticed by the respective weight loss.

#### 3.1.3. Nitrogen adsorption-desorption isotherms

Table 1 summarizes the textural characterization for graphene oxide,  $\text{TiO}_2$  and all prepared GOT composites, including those treated at various temperatures.

In particular, the  $\text{N}_2$  adsorption-desorption isotherms for graphene oxide,  $\text{TiO}_2$  and GOT composites (3.3 wt.% and 12.0 wt.%)

**Table 1**

Textural characterization of P25 and the prepared materials: apparent ( $S_{\text{BET}}$ ) and cumulative mesopore ( $S_{\text{BJH}}$ ) surface area; micropore volume ( $V_{\text{micro}}$ ); and mesopore volume ( $V_{\text{meso}}$ ).

Sample	$S_{\text{BET}}$ ( $\text{m}^2 \text{ g}^{-1}$ )	$S_{\text{BJH}}$ ( $\text{m}^2 \text{ g}^{-1}$ )	$V_{\text{micro}}$ ( $\text{cm}^3 \text{ g}^{-1}$ )	$V_{\text{meso}}$ ( $\text{cm}^3 \text{ g}^{-1}$ )
Graphene oxide	21	—	—	—
P25	65	54	0.03	0.20
TiO <sub>2</sub> -nt	126	24	0.05	0.02
TiO <sub>2</sub> -200	118	47	0.05	0.05
GOT-1.2-nt	79	43	0.03	0.06
GOT-1.2-200	57	58	0.02	0.08
GOT-3.3-nt	136	42	0.06	0.10
GOT-3.3-200	117	107	0.05	0.18
GOT-3.3-350	45	70	0.02	0.25
GOT-4.0-nt	148	47	0.06	0.11
GOT-4.0-200	110	90	0.05	0.14
GOT-5.4-nt	226	79	0.10	0.15
GOT-5.4-200	146	136	0.08	0.20
GOT-8.0-nt	310	157	0.14	0.22
GOT-8.0-200	210	242	0.09	0.36
GOT-12.0-nt	351	174	0.15	0.20
GOT-12.0-200	203	229	0.08	0.31
GOT-12.0-350	116	191	0.05	0.36

(nt) samples not thermally treated.

not submitted to the thermal treatment and treated at 200 °C are shown in Fig. 3(a, b). The theoretical surface area of an individual (reduced) graphene sheet is ca. 2600 m<sup>2</sup> g<sup>-1</sup> [1], while the measured  $S_{\text{BET}}$  for graphene oxide was 21 m<sup>2</sup> g<sup>-1</sup>. A low experimental  $S_{\text{BET}}$ , in comparison with the theoretical  $S_{\text{BET}}$ , is usually reported in literature and related to the stretched assembly of the graphene oxide sheets, originated by strong hydrogen bonding [39] when the suspension is dried to perform the N<sub>2</sub> adsorption analysis.

The N<sub>2</sub> adsorption isotherm of TiO<sub>2</sub>-nt (Fig. 3a) can be classified as type-I [64], typical of microporous materials. When the TiO<sub>2</sub>-nt was treated at 200 °C (TiO<sub>2</sub>-200, Fig. 3b) a change in the adsorptive behaviour, and consequently in the N<sub>2</sub> isotherm, can be detected. In this case, a progressive increase of adsorbed N<sub>2</sub> to higher relative pressures is indicative of adsorption in wide micropores and mesopores. The increase of the micropore and mesopore volume is likely due to increase of the interstitial space between crystallites of TiO<sub>2</sub> during the thermal treatment. For GOT composites, and in particular for a higher GO content of 12 wt.% (Fig. 3a, b), N<sub>2</sub> isotherms can be described as type-IV, which are characteristic of mesoporous materials. In general, GOT composites not treated and treated at 200 °C presented micropore volume,  $S_{\text{BET}}$  and mesopore volume values higher than P25 (Table 1). These values increased with the content of graphene oxide, the highest  $S_{\text{BET}}$  and micropore volume being obtained for GOT-12.0-nt (351 m<sup>2</sup> g<sup>-1</sup> and 0.15 cm<sup>3</sup> g<sup>-1</sup>, respectively), the  $S_{\text{BET}}$  being significantly higher than that measured for graphene oxide, evidencing that a pronounced porosity is created when GO sheets and TiO<sub>2</sub> are in contact, in comparison with the respective single materials. During the thermal treatments of GOT composites, the decrease of the micropore volume and  $S_{\text{BET}}$  (e.g.,  $S_{\text{BET}}$  of 351 and 203 m<sup>2</sup> g<sup>-1</sup> for GOT-12-nt and GOT-12-200, respectively) and the increase of the mesopore volume and  $S_{\text{BJH}}$  (e.g.,  $S_{\text{BJH}}$  of 174 and 229 m<sup>2</sup> g<sup>-1</sup> for GOT-12-nt and GOT-12-200, respectively) should be due to the progressive increase of the TiO<sub>2</sub> particle size and the release of the oxygenated surface groups with the temperature, which produce an enlargement of the interstitial space that becomes of similar sizes to those of mesopores or wider pores. These effects were more evident when samples were treated at 350 °C.

### 3.1.4. Scanning electron microscopy (SEM) and high resolution electron microscopy (HRTEM)

The representative SEM images of TiO<sub>2</sub>-200, GOT-3.3-200 and GOT-12.0-200 are shown in Fig. 4a–b, c–d, and e–f, respectively, for a lower (a, c, e) and a higher (b, d, f) magnification. The morphology

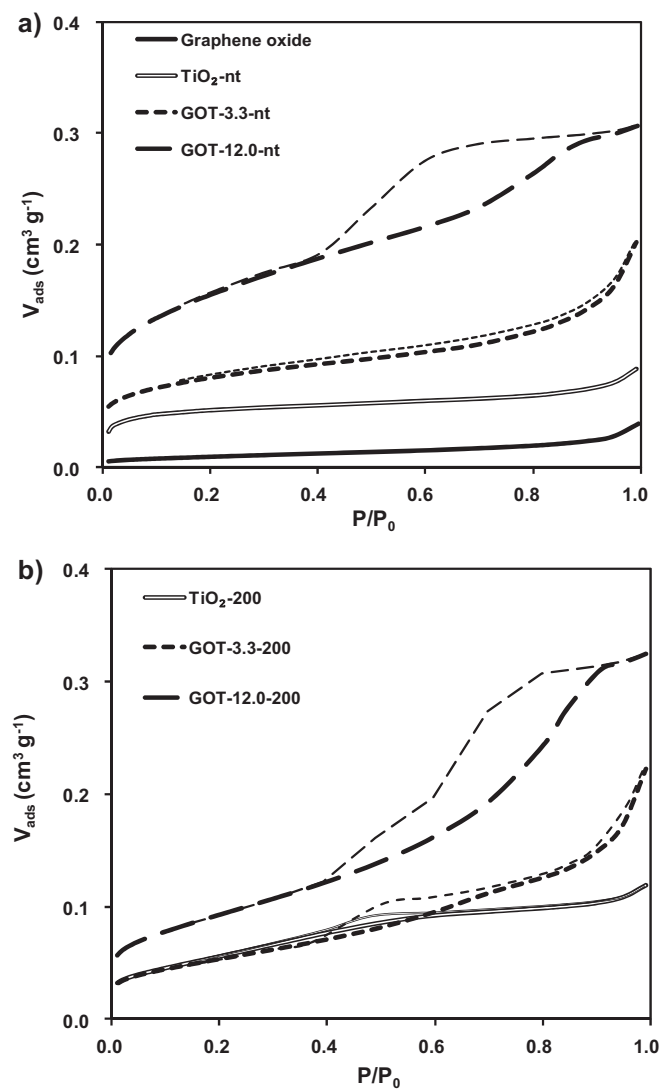


**Fig. 3.** N<sub>2</sub> adsorption–desorption isotherms at −196 °C for (a) graphene oxide, TiO<sub>2</sub>-nt, GOT-3.3-nt and GOT-12.0-nt before heat-treatment; (b) TiO<sub>2</sub>-200, GOT-3.3-200 and GOT-12.0-200 composite after heat treatment at 200 °C.  $V_{\text{ads}}$  is the amount of N<sub>2</sub> adsorbed expressed as volume of liquid.

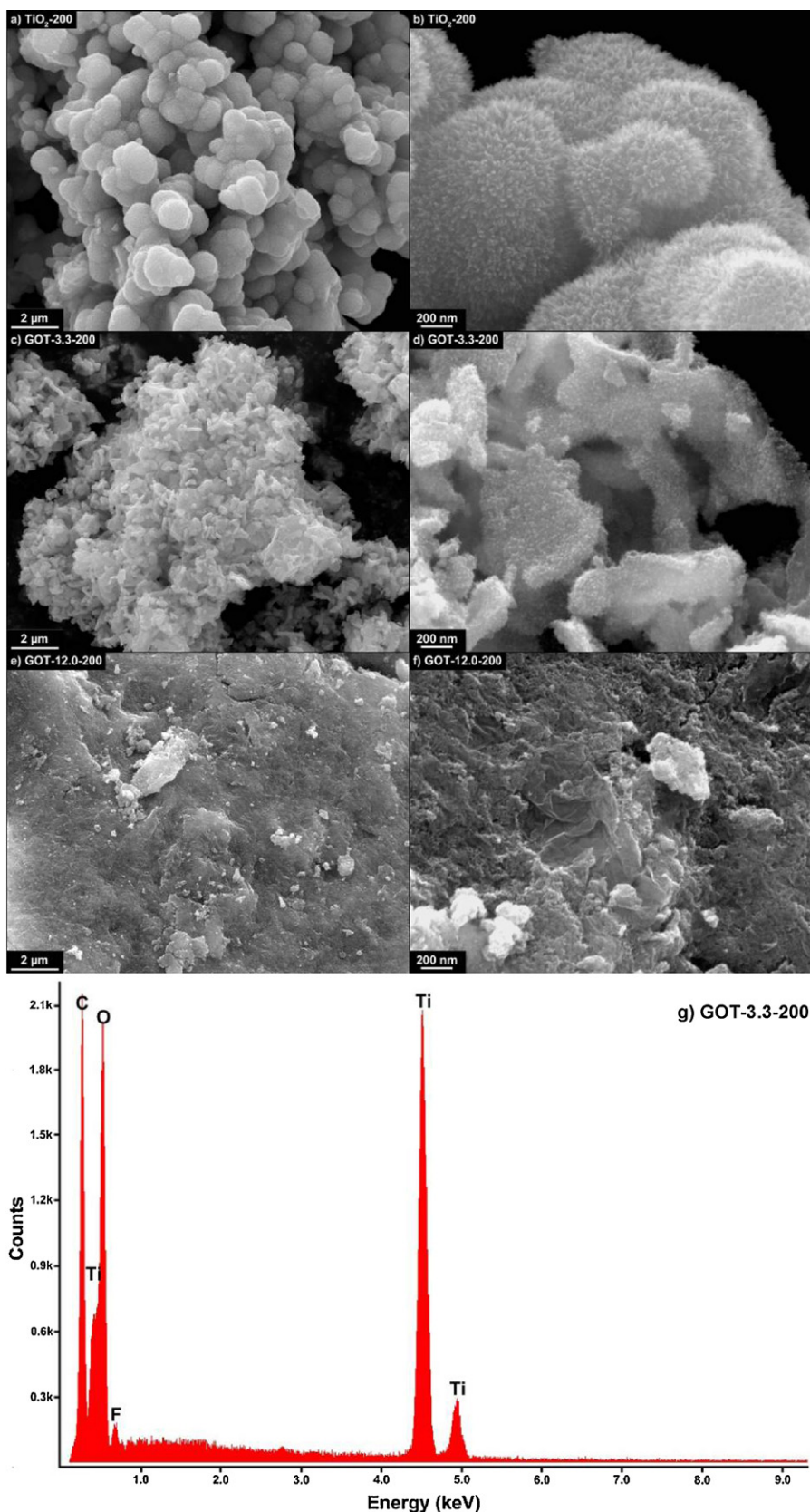


**Fig. 4.** SEM micrographs of (a, b)  $\text{TiO}_2$ -200, (c, d) GOT-3.3-200 and (e, f) GOT-12.0-200, (g) EDX spectrum of GOT-3.3-200.

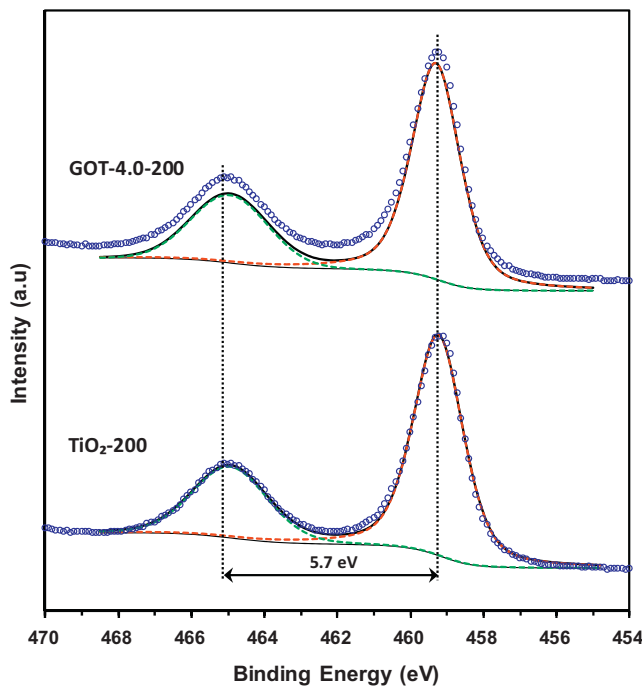


**Fig. 5.** XPS spectra of the Ti2p region for GOT-4.0-200 composite and TiO<sub>2</sub>-200.

of TiO<sub>2</sub>-200 significantly differed from the GOT composites. Fig. 4a, b shows that spherical-like TiO<sub>2</sub> particles aggregate to form larger particles. The GOT-3.3-200 composite (Fig. 4c, d) seems to consist of TiO<sub>2</sub> particles aggregated on the top of graphene oxide layers, forming a kind of junction of GOT platelets. In this case, a well TiO<sub>2</sub> distribution on both sides of the graphene oxide nanosheets seems to occur, indicating a good self-assembly of the TiO<sub>2</sub> nanoparticles on graphene oxide during the preparation method. The morphology found for the composite prepared with higher content of graphene oxide (GOT-12.0-200, Fig. 4e, f) is quite different, larger and rigid agglomerates seem to be formed in this case with a rough surface and even with some uncoated graphene oxide platelets. The morphology observed for GOT-12.0-200 was also observed for GOT-8.0-200 (not shown), while for composites with lower graphene oxide contents (4.0 wt.% and 5.4 wt.%, not shown) the morphology was more similar to the observed for GOT-3.3-200.

These different morphologies could be then related with the amount of graphene oxide nanosheets in suspension and the respective degree of dispersion, a large amount of graphene oxide leading to rigid aggregates with poor and non-uniform assembly of TiO<sub>2</sub> nanoparticles on their surface. EDX spectra of all investigated GOT samples have revealed peaks of Ti, O, C and F. Fig. 4g shows the EDX spectrum of GOT-3.3-200 as an example. The presence of Ti and O atoms corroborates the formation of TiO<sub>2</sub>. The presence of residual F results from the precursor used in the preparation of TiO<sub>2</sub>, and the peak of C can be related to graphene oxide, even if some interference could result from the carbon tape used to fix the sample for SEM analysis.

The morphologies of bare TiO<sub>2</sub> and GOT composites were also characterized by HRTEM (not shown). HRTEM micrographs confirmed TiO<sub>2</sub> spherical particles with a size of 4–5 nm, well in agreement with the Raman results (Section 3.1.7). In addition, selected-area electron diffraction (SAED) performed during HRTEM showed that TiO<sub>2</sub> is present as anatase crystalline phase.

### 3.1.5. X-ray photoelectron spectroscopy (XPS)

Fig. 5 collects XPS spectra of the Ti2p region for GOT-4.0 composite and TiO<sub>2</sub> treated at 200 °C. From deconvolution of the

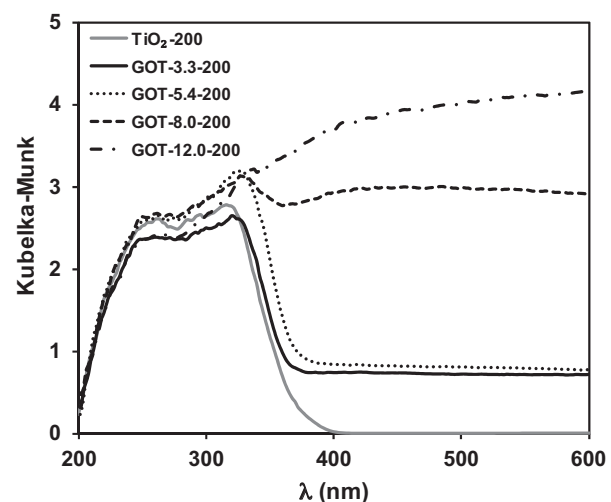


**Fig. 6.** Diffuse reflectance UV-Vis spectra of TiO<sub>2</sub> and GOT composites treated at 200 °C.

Ti2p region, two peaks were detected and centred at 459.1 and 464.8 eV, corresponding to Ti2p<sub>3/2</sub> and Ti2p<sub>1/2</sub>, respectively. In addition, the splitting between both peaks was found at 5.7 eV. These results indicate a Ti<sup>4+</sup> chemical state, typical of TiO<sub>2</sub> in graphene oxide-TiO<sub>2</sub> composites [34]. In addition, the comparable binding energies found for both GOT-4.0-200 and TiO<sub>2</sub>, and the absence of peaks at 465.8 and 460.2 eV, suggest that TiO<sub>2</sub> is not doped with carbon [65].

### 3.1.6. Diffuse reflectance UV-Vis spectroscopy

Diffuse reflectance (DR) UV-Vis spectra for TiO<sub>2</sub>-200 and some GOT composites with different graphene oxide contents are shown in Fig. 6. All GOT composites absorb in the whole visible region of the spectrum, as observed for other carbonaceous materials combined with TiO<sub>2</sub> [26,66–68]. Thereby the absorption edge of TiO<sub>2</sub> upon the addition of graphene oxide indicates a band-gap narrowing, which could be attributed to the chemical bonding between TiO<sub>2</sub> and the specific sites of carbon (Ti—O—C bond) similar to that found for P25-GO composites [37,41]. This effect is proportional to the graphene oxide content, a weaker absorption in the visible region being observed for the composites with lower amount of graphene oxide. It is quite difficult to determine reliable values for the band gaps of samples prepared with GO, in particular for those samples with higher GO content, due to the significant background absorption increase above 400 nm. Even so, the band gaps determined for the GOT composites (e.g., 2.98, 2.95, and 2.90 for GOT-1.2-200, GOT-3.3-200 and GOT-5.4-200, respectively) were lower than for bare TiO<sub>2</sub> (3.12).

### 3.1.7. Raman spectroscopy

To investigate the structural properties of the GOT composites and electronic coupling between graphene oxide and TiO<sub>2</sub>, we have employed Raman spectroscopy that has been established as a powerful method for the characterization of carbon nanomaterials [69,70]. Fig. 7 displays the Raman spectra of the GOT composites compared with the bare GO suspension and TiO<sub>2</sub>-200 at 514.5 and 785 nm excitations. At 514.5 nm, pristine GO exhibited the graphitic Raman G band at 1603 cm<sup>-1</sup> arising from the bond stretching of sp<sup>2</sup> carbon atoms and the defect activated D band at 1346 cm<sup>-1</sup> together with its 2D overtone at 2694 cm<sup>-1</sup> (G' band), the defect activated combination mode (D+G) at 2939 cm<sup>-1</sup> and the 2G overtone at 3182 cm<sup>-1</sup>. All these Raman modes were superimposed on the high energy tail of the broad photoluminescence (PL) background of GO that spans the visible to the NIR spectral

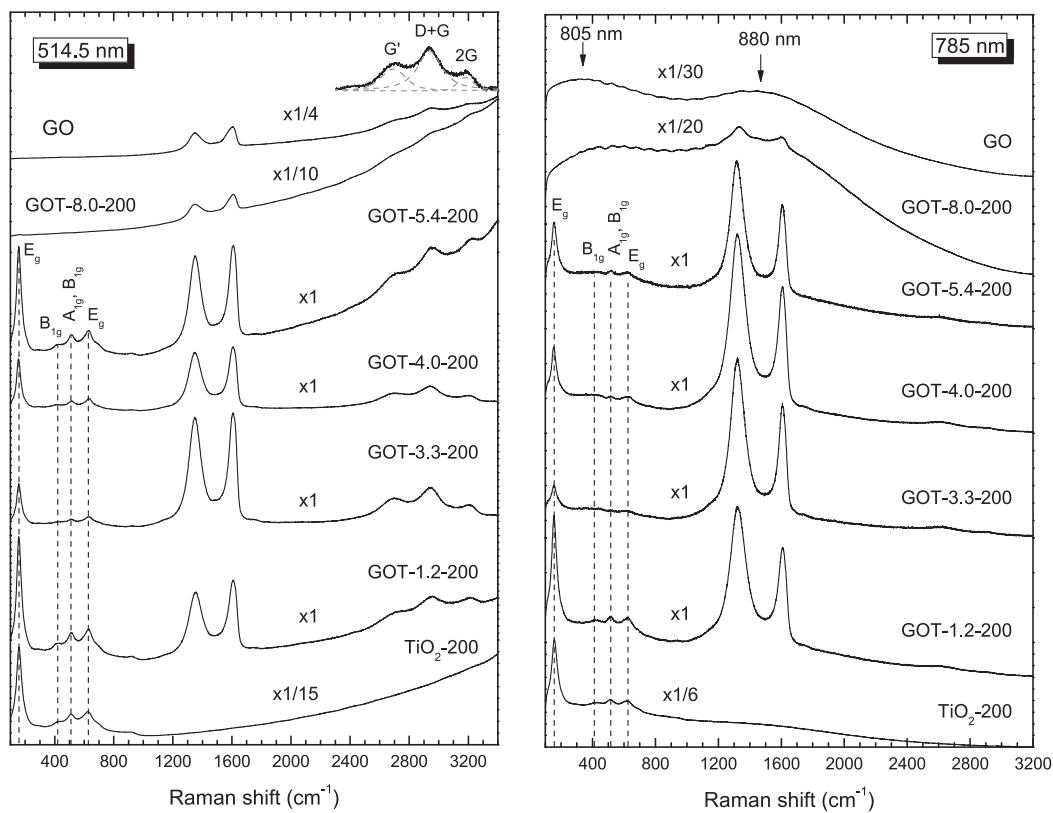


**Fig. 7.** Raman spectra of the GOT composites compared with the GO suspension and  $\text{TiO}_2$ -200 at 514.5: (left) and 785 nm (right) excitations. Broken lines depict the anatase Raman modes. The upper inset shows the deconvolution of the second order GO modes after subtraction of the PL background.

range [71–73]. At 785 nm, the intense PL of GO, which can be associated with the radiative electron–hole recombination of localized  $\text{sp}^2$  clusters in the  $\text{sp}^3$  C–O matrix of GO [72], yields two broad local maxima at 805 and 880 nm that mask completely the GO Raman peaks. However, in situ deposition of  $\text{TiO}_2$  nanoparticles on the GO sheets resulted in the gradual suppression of the intense GO emission allowing the clear identification of the GO and  $\text{TiO}_2$  Raman bands at both excitation wavelengths (Fig. 7).

The broad and asymmetric G band of GO ( $1603\text{ cm}^{-1}$ ) exhibited considerable blue shift compared to that of pure graphite ( $1582\text{ cm}^{-1}$ ), which can be related to the contribution of an alternating pattern of single-double carbon bonds within the  $\text{sp}^2$  ribbons of GO [74] or alternatively the merging with the higher frequency ( $\sim 1620\text{ cm}^{-1}$ ) defect activated D' band [75] upon the introduction of high amounts of disorder on the graphene planes, as can be inferred from recent studies on single layer graphene treated by oxygen plasma [76] and Ar ion bombardment [77]. Binding of GO with  $\text{TiO}_2$  resulted in additional blue shift of both the G and D bands by  $3\text{--}5\text{ cm}^{-1}$  along with appreciable narrowing ( $10\text{--}15\text{ cm}^{-1}$ ) for the GOT composites, as shown in Fig. 8a, in contrast to the red-shifted G band that was previously noted in thermally reduced GO [73,74]. In addition, the intensity ratio  $I_{\text{D}}/I_{\text{G}}$  derived from the integrated areas of the D and G bands, which is the characteristic probe of the size of  $\text{sp}^2$  clusters as well as of the defect density in graphitic materials [69,75], increased for the GOT composites by approximately 20%, though no systematic dependence on the GO content was observed (Fig. 8a). Previous studies have shown that thermal reduction of GO usually results in minor changes of the  $I_{\text{D}}/I_{\text{G}}$  intensity ratio [78–80], consistently with the creation of new  $\text{sp}^2$  clusters that serve as percolation pathways between pre-existing nanometric  $\text{sp}^2$  graphitic domains upon the initial stages of oxygen removal from GO [79]. The observed variation of the G and D bands in the GOT composites could be then primarily ascribed to the anchoring

of the  $\text{TiO}_2$  nanoparticles that act as defects on the surface of the GO sheets, which retain their structural integrity upon liquid phase deposition of  $\text{TiO}_2$ .

Similarly, the presence of  $\text{TiO}_2$  nanoparticles was identified for all the GOT composite materials by their distinct Raman bands at lower frequencies ( $100\text{--}700\text{ cm}^{-1}$ ) for both excitation wavelengths (Fig. 7). The most intense Raman-active modes of the anatase phase were detected at  $158$  ( $E_{\text{g}(1)}$ ),  $430$  ( $B_{1\text{g}}$ ),  $510$  (superposition of  $A_{1\text{g}}$  and  $B_{1\text{g}}$ ) and  $626\text{ cm}^{-1}$  ( $E_{\text{g}}$ ), with minor frequency shifts between the GOT composites and the reference  $\text{TiO}_2$ -200 sample. Both the frequency and the width of these Raman modes are markedly different from those of bulk anatase, a characteristic feature of optical phonon confinement that leads to the broadening and shift of the Raman bands in nanosized  $\text{TiO}_2$  [81]. Relying on the peak position ( $158\text{ cm}^{-1}$ ) and full-width at half-maximum-FWHM ( $40\text{ cm}^{-1}$ ) of the lowest frequency  $E_{\text{g}}$  mode and the linear scaling of the Raman shift versus FWHM derived for the phonon confinement effect [81,82], we estimate the size of the anatase  $\text{TiO}_2$  nanocrystals grown on GO by LPD to be  $\sim 4\text{ nm}$ .

However, while both  $\text{TiO}_2$  and GO components essentially preserve their Raman characteristics in the GOT composites, the most insightful feature on the GO– $\text{TiO}_2$  interaction is the gradual evolution of the PL background with the GO content. Specifically, the strong PL of pristine GO was found to persist for GOT-8.0-200 at both visible and NIR laser excitations (Fig. 7). This suggests the presence of abundant GO emissive species stemming from the excess of GO that leaves partially coated or even uncoated GO platelets, according to the SEM results. Further decrease of the GO content resulted in the progressive reduction of the PL background and its reappearance at the lowest GO content. To quantify the relative PL variation we have employed the slope of the PL background ( $m$ ) to the intensity of the G band  $I_{\text{G}}$  at  $514.5\text{ nm}$ , which is often used as a quantitative probe of the PL strength in

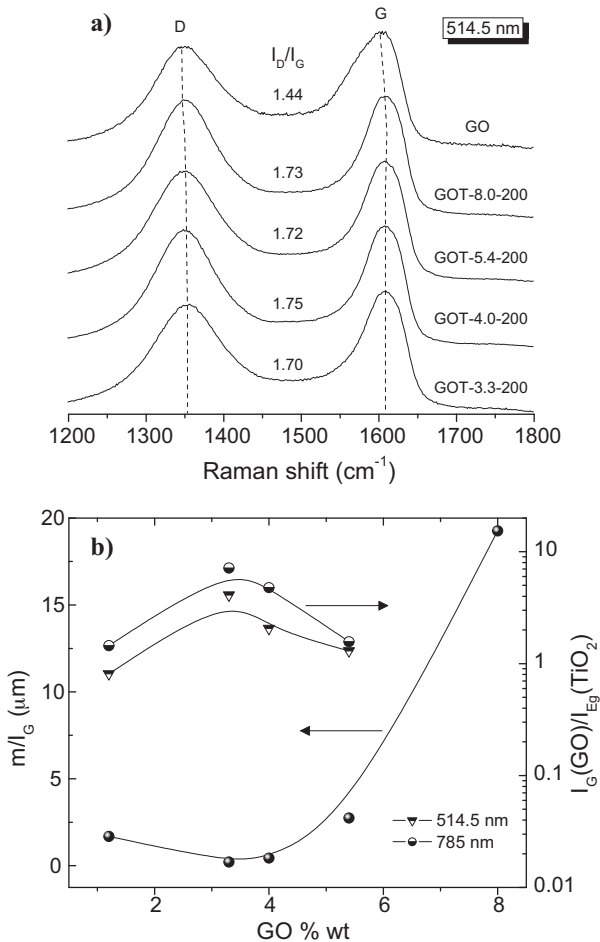


**Fig. 8.** (a) Evolution of the D to G band ratio as a function of the GO content at 514.5 nm. (b) The corresponding GO dependence of the PL background slope ( $m$ ) to the G peak intensity ( $I_G$ ) ratio (left axis) and of the intensity area ratio of the G band to the low frequency  $E_g$  anatase mode  $I_G(GO)/I_{Eg}(TiO_2)$  (right axis).

disordered carbons [83]. Fig. 8b shows the corresponding ratio  $m/l_G$  for the different GOT composites, which was calculated from the linear fitting of the PL background in the range of 1000–2000 cm<sup>-1</sup> and  $I_G$  that was taken from the height and not the area of the G peak, for consistency with previous results [76,83]. The evolution of  $m/l_G$  exhibited a continuous decrease with the GO content down to 3.3–4.0 wt.%, where almost complete quenching of the GO PL is reached, followed by a weak rise at lower GO content, where the self-emission of the TiO<sub>2</sub> nanoparticles may also contribute. This behavior was further mirrored in the variation of the GO/TiO<sub>2</sub> relative Raman intensity for the different GOT composites, monitored by the intensity area ratio of the G band to the low frequency  $E_g$  anatase mode  $I_G(GO)/I_{Eg}(TiO_2)$ , as shown in Fig. 8b. The latter ratio exhibited a local maximum at 3.3–4.0 wt.% simultaneously with the quenching of the GO PL, in contrast to the continuous decrease that would be expected based on the corresponding GO mass ratio. Most importantly, the non-monotonous variation of the GO PL correlated perfectly with the evolution of the GOT photocatalytic activity, where optimum performance was attained for the same GOT compositions at both near UV–Vis and visible light irradiation (Section 3.2), implying a common origin of the underlying effects.

In fact, the observed PL quenching in the GOT composites resembles closely the interplay of Raman and PL in quantum dot sensitized TiO<sub>2</sub>, where interfacial electron transfer from the anchored quantum dots to TiO<sub>2</sub> was realized under visible light

excitation [84]. The present results indicate that photo-generated electrons in the thermally reduced GO under visible or NIR laser excitation can be efficiently transferred to the surface bound TiO<sub>2</sub> nanoparticles before radiative recombination [72] and thus inhibit charge recombination in the GOT composites and promote their photocatalytic activity under visible light (Section 3.2).

Evidence for such a charge transfer mechanism has been recently provided by both theoretical calculations of the graphene/TiO<sub>2</sub> interface and photocurrent spectra in GO/TiO<sub>2</sub> nanocomposites [38,51], where the large difference between the corresponding work functions was found to shift markedly the graphene Fermi level, enabling transfer of electrons from graphene into the TiO<sub>2</sub> conduction band under visible light irradiation. It should be noted that this type of interfacial interaction, that is operative under visible light, should be differentiated from the action of GO as a scavenger and transporter of photo-generated electrons in TiO<sub>2</sub> under UV excitation, which has been mainly implicated to explain the UV photocatalytic and/or photoelectrochemical performance enhancement in GO/TiO<sub>2</sub> nanocomposites [31,32]. In fact, the inherent spatial inhomogeneity in the size of aromatic sp<sup>2</sup> domains in reduced GO [72], and the concomitant variation of the corresponding localized  $\pi$  and  $\pi^*$  energy states spanning the visible to the NIR spectra range, may enable electron transfer to and from TiO<sub>2</sub> in the GO–TiO<sub>2</sub> composites, depending on the excitation energy. In that case, GO could act either as an electron acceptor and shuttle, or as an electron donor under UV and visible light, respectively, depending on the relative position of the sp<sup>2</sup> energy levels with respect to the conduction band of TiO<sub>2</sub>. The possibility of such a hybrid charge transfer process is further corroborated by the distinct effects of hole and radical scavengers in the photocatalytic activity of the GOT composites under near UV/Vis compared to visible light irradiation (Section 3.2.3).

The effect of the thermal treatment on the structural properties and GO–TiO<sub>2</sub> coupling was subsequently investigated by comparing the Raman spectra of the GOT composites before and after calcination in N<sub>2</sub> flow. Fig. 9a shows representative Raman spectra for the GOT-3.3nt, GOT-3.3-200 and GOT-3.3-350 composites at 514.5 nm. Calcination at higher temperature resulted in the narrowing and red-shift of the anatase Raman bands, especially at 350 °C (left inset of Fig. 9a), a distinctive feature of the growth of anatase crystallites and the partial release of the optical phonon confinement effect [85]. Specifically, the lowest frequency anatase  $E_g$  mode was detected at frequencies and FWHM (in parentheses) of 161(50), 158(40), and 149(20) cm<sup>-1</sup> for the GOT-3.3nt, GOT-3.3-200 and GOT-3.3-350 composites, respectively, corresponding to an increase of the anatase crystallite size from ~3 to 6 nm. Apart from the enhancement of TiO<sub>2</sub> crystallinity, thermal treatment resulted in the red-shift of the D band and a moderate increase of the  $I_D/I_G$  ratio with the increase of the calcination temperature. This behaviour was most prominent at 785 nm, where the relative D band intensity is greatly enhanced (right inset of Fig. 9a) [75], and can be related to the progressive release of the GO oxygen groups that mediate the GO–TiO<sub>2</sub> binding and the simultaneous size increase of the anatase nanoparticles acting as defects on the GO sheets. In addition, the GO/TiO<sub>2</sub> relative intensity probed through the  $I_G(GO)/I_{Eg}(TiO_2)$  ratio systematically decreased with calcination, reflecting the gradual GO weight loss (Fig. 9b).

On the other hand, while the GO emission detected through the ratio  $m/l_G$  was quenched after thermal treatment at 200 °C, indicative of optimal electron transfer and thus GO–TiO<sub>2</sub> binding, an upsurge was observed at 350 °C (Fig. 9c). The increased removal of oxygen groups at 350 °C can be accordingly inferred to disrupt the anchoring of the larger TiO<sub>2</sub> nanoparticles on GO and thus to contribute in the increase of the concentration of PL species upon higher thermal reduction.

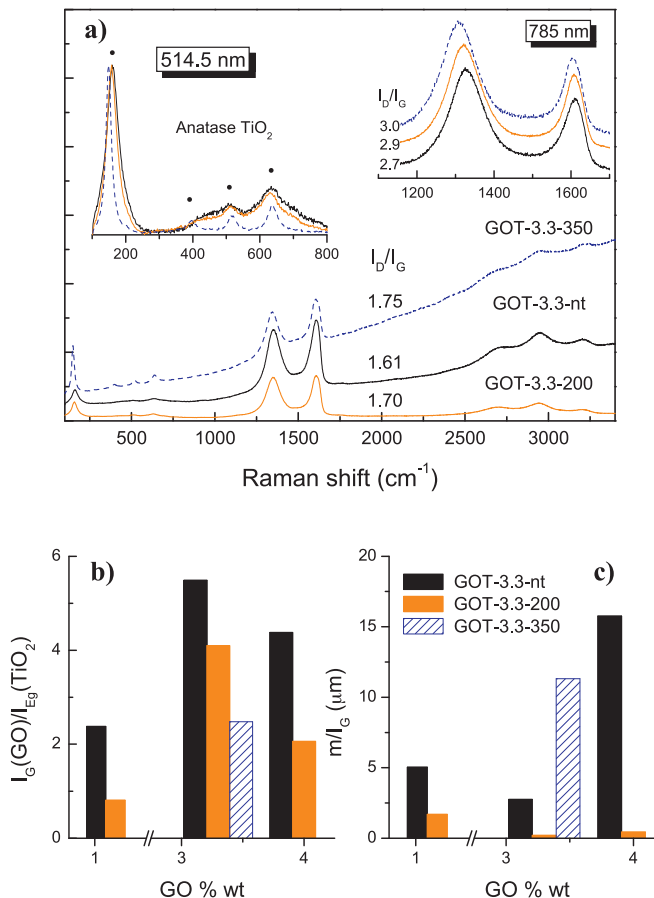


**Fig. 9.** (a) Raman spectra for the GOT-3.3nt, GOT-3.3-200 and GOT-3.3-350 composites at 514.5 nm. The insets show in detail the corresponding normalized Raman spectra of the anatase  $\text{TiO}_2$  modes at 514.5 nm (left) and the G and D bands of GO at 785 nm (right). (b) The variation of the  $I_G(\text{GO})/I_{Eg}(\text{TiO}_2)$  intensity ratio for the 1.2 wt.%, 3.3 wt.% and 4.0 wt.% GOT composites as a function of thermal treatment. (c) The corresponding variation of the  $m/l_G$  ratio at 514.5 nm.

### 3.2. Photocatalytic experiments

#### 3.2.1. DP photocatalytic degradation

The composites obtained by the LPD method with different graphene oxide contents and temperatures of treatment, as well as the  $\text{TiO}_2$ -200 and benchmark P25 materials, were tested in the photodegradation of DP under near-UV/Vis (Fig. 10a, b) and visible light (Fig. 10c) irradiation. The respective pseudo-first order rate constants are gathered in Table 2 and for GOT composites the results are also represented in Fig. 10d (closed circles). The direct photolysis of DP in aqueous solutions was first investigated in order to quantify the DP degraded under non-catalytic conditions. DP is a very resistant pollutant in the absence of a catalyst, since less than 6% of DP conversion in 60 min was obtained under near-UV/Vis irradiation (Fig. 10a). Moreover, in the dark, single graphene oxide induces a significant 36% reduction of the DP concentration (not shown), indicative of its adsorption capability, while in the case of GOT composites the adsorption of DP concentration in the dark decreases with the graphene oxide content, being obtained around 5% and 15% for GOT-1.2-200 and GOT-12-200, respectively, in accordance with their  $S_{\text{BET}}$  (Table 1).

The photocatalytic efficiency of the tested materials treated at 200 °C for DP degradation under near-UV/Vis irradiation follows the order (Fig. 10a, b): GOT-3.3-200 ( $62.3 \times 10^{-3} \text{ min}^{-1}$ ) > GOT-4.0-200 ( $60.0 \times 10^{-3} \text{ min}^{-1}$ ) > P25 ( $56.4 \times 10^{-3} \text{ min}^{-1}$ ) > GOT-5.4-200 ( $45.5 \times 10^{-3} \text{ min}^{-1}$ ) > GOT-8.0-200 ( $24.8 \times 10^{-3} \text{ min}^{-1}$ ) > GOT-1.2-200 ~ GOT-12.0-200 ( $18.1 \times 10^{-3} \text{ min}^{-1}$ ) >  $\text{TiO}_2$ -200 ( $16.8 \times 10^{-3} \text{ min}^{-1}$ ), where the values in brackets refer to the pseudo-first order rate constants (Table 2).

Therefore, any amount of graphene oxide in the GOT composites leads to higher pseudo-first order rate constants for DP degradation (from  $18.1 \times 10^{-3}$  to  $62.3 \times 10^{-3} \text{ min}^{-1}$ ) than that observed for the bare  $\text{TiO}_2$  material prepared in this work ( $16.8 \times 10^{-3} \text{ min}^{-1}$ ). It can be also noticed that no appreciable DP degradation was observed for the composite containing 1.2 wt.% of graphene oxide, the pseudo-first order rate constant being similar for the graphene oxide content of 12.0 wt.% ( $18.1 \times 10^{-3} \text{ min}^{-1}$ ). A clear decrease in the pseudo-first order rate constant, from  $62.3 \times 10^{-3}$  to  $18.1 \times 10^{-3} \text{ min}^{-1}$ , is related with the increase in the graphene oxide content, from 3.3 wt.% to 12 wt.%, respectively. Fig. 10d clearly shows that the optimal graphene oxide content in terms of DP degradation under near-UV/Vis irradiation is around 3.3–4.0 wt.%, in perfect agreement with the best GOT composition range in terms of charge transfer inferred from the PL quenching of graphene oxide identified in the Raman spectra (Fig. 7b). These results point to a synergistic effect between the graphene oxide layers and  $\text{TiO}_2$  nanoparticles, which depends on the graphene oxide content, whose control is crucial to obtain highly efficient photocatalysts.

In general, the associated mineralization shows a very similar trend (Fig. 11). In particular, after 60 min of near-UV/Vis irradiation, the composites prepared with graphene oxide content of 3.3 wt.% and 4.0 wt.% produced a TOC reduction of 50% and 55%, respectively, while graphene oxide contents of 1.2%, 5.4%, 8.0%, and 12.0% led to TOC reductions of 25% 46%, 30% and 27%, respectively. Therefore, since the results were quite similar in terms of DP degradation for composites prepared with 3.3 wt.% and 4.0 wt.% ( $k = 62.3 \times 10^{-3}$  and  $60.0 \times 10^{-3} \text{ min}^{-1}$ , respectively), as well as in terms of TOC reduction (50% and 55%, respectively), it is possible to conclude that the optimal graphene oxide content under near-UV/Vis irradiation is ca. 3.3–4.0 wt.%. In fact, both composites are highly active under near-UV/Vis irradiation (nearly complete degradation of DP is achieved in 60 min), the observed activity being even slightly higher than that obtained for the benchmark P25 photocatalyst (pseudo-first order rate constant of  $56.4 \times 10^{-3} \text{ min}^{-1}$  and 48% of TOC reduction).

Fig. 10a also shows the results obtained with the GOT-3.3-nt and GOT-3.3-350 composites. It was found that the photocatalytic activity of GOT prepared with 3.3 wt.% of graphene oxide increases when thermal treatment is applied at 200 °C but decreases if performed at 350 °C ( $k = 45.7 \times 10^{-3}$ ,  $62.3 \times 10^{-3}$  and  $29.7 \times 10^{-3} \text{ min}^{-1}$  for GOT-3.3-nt, GOT-3.3-200 and GOT-3.3-350, respectively), showing that the photocatalytic activity of the GOT composites is clearly influenced by the calcination temperature. In fact, thermal reduction at 200 °C improves considerably the photocatalytic activity of the composites by improving of the graphene oxide conductivity [79] as well as enhancing of the electronic coupling of the GO sheets with the  $\text{TiO}_2$  nanoparticles, evidenced by the reduction of the corresponding PL emission (Fig. 9). On the other hand, thermal treatment at 350 °C results in a marked (two fold) decrease of the photocatalytic activity, despite the growth and improved crystallinity of the  $\text{TiO}_2$  nanoparticles, which was verified by Raman spectroscopy. This effect can be rationalized by the removal of the oxygenated surface groups of graphene oxide at low temperatures, as observed by TG/DTG (Fig. 2). Since these groups mediate the efficient and uniform assembly of the  $\text{TiO}_2$  nanoparticles on the graphene oxide sheets, their removal is expected to dismantle partially the GOT composite structure (as observed by FESEM, not shown) and to disrupt the binding and charge transfer between graphene oxide and  $\text{TiO}_2$ , as inferred from the concomitant reappearance of the PL emission for GOT-3.3-350 (Fig. 9). Therefore the temperature of treatment and the graphene oxide content are important parameters for improving the photocatalytic performance of the GOT materials.

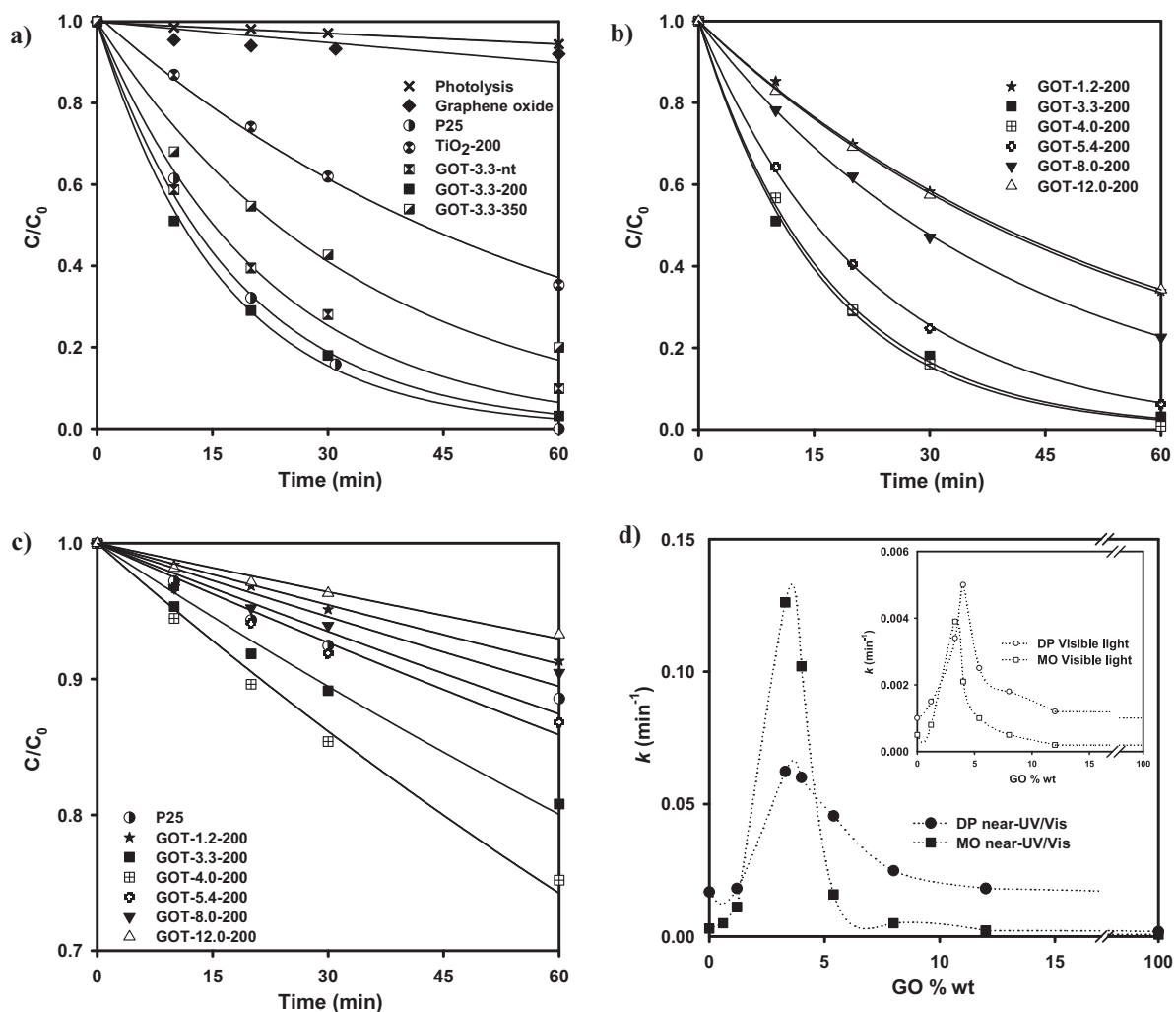


**Fig. 10.** Photocatalytic degradation of DP ( $100 \text{ mg L}^{-1}$ ) for (a) graphene oxide,  $\text{TiO}_2$ -200, P25 and GOT-3.3-nt and treated at  $200^\circ\text{C}$  and  $350^\circ\text{C}$  under near-UV/Vis, (b) composites with different content of graphene oxide under near-UV/Vis, (c) composites with different content of graphene oxide under visible light irradiation, (d) pseudo-first order reaction rate constant ( $k$ ) under near-UV/Vis and visible light irradiation for DP and MO. Catalyst load =  $1.0 \text{ g L}^{-1}$ . Curves represent the fitting of the pseudo-first order equation to the experimental data.

**Table 2**

Pseudo first-order kinetic rate constant ( $k$ ) and regression coefficient ( $r^2$ ) of DP and MO degradation under near-UV/Vis and visible irradiation at different conditions.

	DP				MO			
	Near-UV/Vis		Visible		Near-UV/Vis		Visible	
	$k \times 10^{-3} (\text{min}^{-1})$	$r^2$	$k \times 10^{-3} (\text{min}^{-1})$	$r^2$	$k \times 10^{-3} (\text{min}^{-1})$	$r^2$	$k \times 10^{-3} (\text{min}^{-1})$	$r^2$
Photolysis	0.90	0.995	n.d.	n.d.	1.00	0.92	n.d.	n.d.
P25	56.4	0.998	2.20	0.97	51.5	0.98	4.50	0.96
$\text{TiO}_2$ -200	16.8	0.997	1.00	0.99	3.00	0.99	1.00	0.98
$\text{TiO}_2$ -200-tBuOH	11.1	0.993	n.d.	n.d.	n.d.	n.d.	n.d.	n.d.
$\text{TiO}_2$ -200-EDTA	2.10	0.93	n.d.	n.d.	n.d.	n.d.	n.d.	n.d.
GOT-1.2-200	18.1	0.9996	1.50	0.998	11.1	0.996	1.50	0.95
GOT-3.3-nt	45.7	0.992	n.d.	n.d.	n.d.	n.d.	n.d.	n.d.
GOT-3.3-200	62.3	0.999	3.40	0.97	126	0.997	7.70	0.98
GOT-3.3-200-tBuOH	28.7	0.994	1.90	0.996	n.d.	n.d.	n.d.	n.d.
GOT-3.3-200-EDTA	6.80	0.98	1.30	0.99	n.d.	n.d.	n.d.	n.d.
GOT-3.3-350	29.7	0.993	n.d.	n.d.	n.d.	n.d.	n.d.	n.d.
GOT-4.0-200	60.0	0.9994	5.00	0.996	102	0.995	4.30	0.993
GOT-5.4-200	45.5	0.9999	2.50	0.98	15.9	0.999	2.60	0.97
GOT-8.0-200	24.8	0.9998	1.80	0.95	5.00	0.995	1.00	0.96
GOT-12.0-200	18.1	0.9998	1.20	0.99	1.00	0.98	0.50	0.96

n.d.: Not determined.

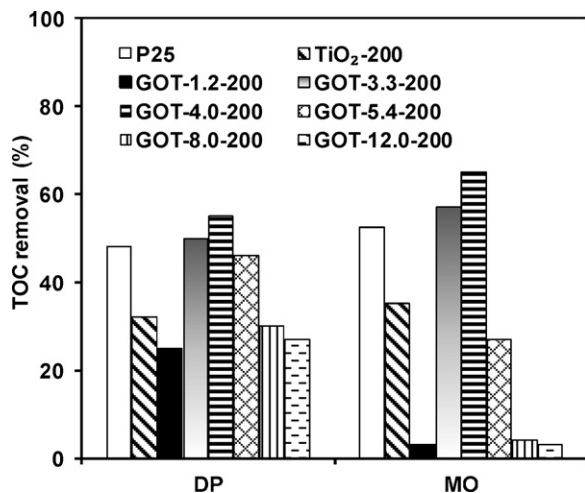


**Fig. 11.** Total organic carbon (TOC) reduction for DP and MO photodegradation under near-UV/Vis irradiation for TiO<sub>2</sub>-200, P25 and different GOT composites treated at 200 °C.

The corresponding results obtained for DP degradation under visible light irradiation are presented in Fig. 10c, Table 2 and in the inset of Fig. 10d (open circles). As expected, the respective pseudo-first order rate constants under visible light irradiation are lower than those obtained under near-UV/Vis irradiation (Table 2), because the same lamp was used in both cases and the cut-off long pass filter just selects the irradiation with  $\lambda > 430$  nm. The efficiency of GOT composites treated at 200 °C under visible light irradiation follows the order: GOT-4.0-200 ( $5.0 \times 10^{-3}$  min<sup>-1</sup>)>GOT-3.3-200 ( $3.4 \times 10^{-3}$  min<sup>-1</sup>)>GOT-5.4-200 ( $2.5 \times 10^{-3}$  min<sup>-1</sup>)>P25 ( $2.2 \times 10^{-3}$  min<sup>-1</sup>)>GOT-8.0-200 ( $1.8 \times 10^{-3}$  min<sup>-1</sup>)>GOT-1.2-200 ( $1.5 \times 10^{-3}$  min<sup>-1</sup>)>GOT-12.0-200 ( $1.2 \times 10^{-3}$  min<sup>-1</sup>), where the values in brackets refer to the pseudo-first order rate constants (Table 2). Once again, the composites prepared with an amount of graphene oxide of 3.3 wt.% and 4.0 wt.% exhibited the higher photocatalytic activities (as also represented in Fig. 10d). In addition, the pseudo-first order rate constants for these GOT materials are significantly higher than that obtained for P25, indicating that GOT composites with optimal content of graphene oxide have extended photocatalytic activity, in comparison with P25, under visible light irradiation; a result of paramount importance for solar applications. Regarding the mineralization obtained under visible light irradiation (not shown), the composites prepared with 3.3 wt.%, 4.0 wt.% and 12 wt.%, produced a 13%, 10% and 2% TOC reduction, respectively, while P25 removed around 5% of the TOC content, reinforcing the higher photocatalytic activity of GOT composites prepared with 3.3 wt.% and 4.0 wt.%.

### 3.2.2. MO photocatalytic degradation

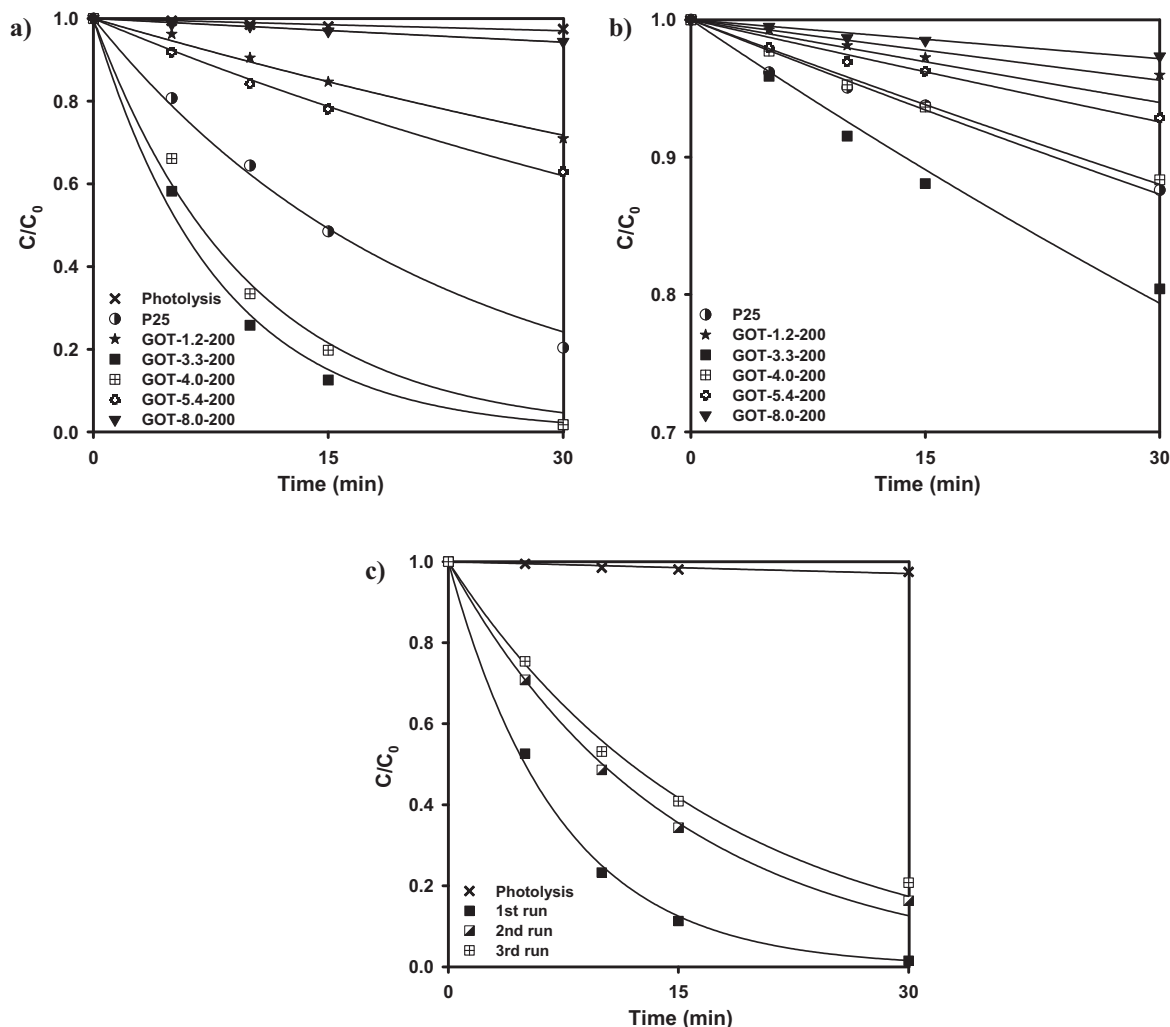
Results reported in literature indicate that GOT composites exhibit extremely high photocatalytic activity towards degradation of azo dyes [34,37,41,63,86,87]. For this reason, as reference, the photocatalytic activity of P25, TiO<sub>2</sub>-200 and different GOT composites prepared in this work was also evaluated for the degradation of MO under both near-UV/Vis and visible light irradiation, as shown in Fig. 12a and b, respectively. The pseudo-first order rate constants are presented in Table 2 and represented in Fig. 10d (closed squares for near-UV/Vis irradiation and open squares in the inset for visible light irradiation).

Fig. 12a shows that MO is poorly degraded in the absence of a catalyst (3% of MO conversion in 30 min), but nearly complete degradation can be achieved within 30 min at a much faster rate than for the DP pharmaceutical (60 min, Fig. 10a)

under near-UV/Vis irradiation at the employed conditions (e.g.,  $k = 126 \times 10^{-3}$  and  $62.3 \times 10^{-3}$  min<sup>-1</sup> for MO and DP, respectively, when GOT-3.3-200 was used). In fact, for MO, the pseudo-first order rate constants under near-UV/Vis irradiation were found as (Table 2): GOT-3.3-200 ( $126 \times 10^{-3}$  min<sup>-1</sup>)>GOT-4.0-200 ( $102 \times 10^{-3}$  min<sup>-1</sup>)>P25 ( $51.5 \times 10^{-3}$  min<sup>-1</sup>)>GOT-5.4-200 ( $15.9 \times 10^{-3}$  min<sup>-1</sup>)>GOT-1.2-200 ( $11.1 \times 10^{-3}$  min<sup>-1</sup>)>GOT-8.0-200 ( $5.0 \times 10^{-3}$  min<sup>-1</sup>). Additionally, the same trend was found concerning the respective TOC reduction (Fig. 11). Under visible light, the highest MO photodegradation was also found for GOT-3.3-200 (Fig. 12b and inset of Fig. 10d), presenting a markedly higher photocatalytic activity than P25 ( $k = 7.7 \times 10^{-3}$  and  $4.5 \times 10^{-3}$  min<sup>-1</sup> for GOT-3.3-200 and P25, respectively).

Overall, a similar trend of the photocatalytic activity for the tested materials was found for both MO and DP in terms of both initial pollutant abatement and TOC reduction. GOT composites prepared with ca. 3.3–4.0 wt.% of graphene oxide content exhibited the highest photocatalytic activity among the GOT materials tested. In addition, these two GOT composites present higher photocatalytic activity than P25 for MO and DP degradation and mineralization, the enhanced activity of GOT composites being less notorious for DP degradation (Fig. 10a) than for MO abatement (Fig. 12a). These results provide firm evidence for the beneficial effect of combining thermally reduced graphene oxide with TiO<sub>2</sub> for the photocatalytic degradation of water pollutants and, in particular, for azo dyes.

The observed enhancement of the photocatalytic activity could be in principle accounted for primarily by the interfacial charge transfer process that can effectively inhibit electron–hole recombination as well as the enhanced capacity of the GOT composites for the physical and chemical adsorption of pollutant molecules [37,86]. Kamat and co-workers [31,32] have shown that photo-generated electrons in UV irradiated TiO<sub>2</sub> can be transferred to GO, thus promoting charge separation under UV irradiation. Such electron transfer from TiO<sub>2</sub> to GO complies energetically with the slightly higher energy of the conduction band edge for TiO<sub>2</sub> ( $-4.2$  eV) with respect to the calculated work function for pristine graphene ( $-4.42$  eV), similar to that of graphite [88,89]. The present results demonstrate that fine tuning of the GO concentration and thermal treatment conditions upon in situ growth of TiO<sub>2</sub> nanoparticles on the graphene oxide sheets is a key aspect for the optimization of the to GO-TiO<sub>2</sub> interface. The ensuing electron transfer from TiO<sub>2</sub> to the graphene sheets can thus rationalize the higher photocatalytic activity obtained for the GOT composites in comparison with bare TiO<sub>2</sub> under UV excitation. However, such an energy level scheme for the graphene oxide/TiO<sub>2</sub> heterojunction, which largely neglects the intrinsically heterogeneous GO electronic structure [30], would also preclude any electron transfer from GO to TiO<sub>2</sub> under visible light excitation. This would further imply that the photocatalytic activity of the GOT composites under visible light is merely due to the dye self-sensitized photocatalytic mechanism that is operative only for the direct self-oxidation of colored pollutants [50], as has been recently proposed for reduced GO-TiO<sub>2</sub> and GO-SnO<sub>2</sub> composites [47]. While such a mechanism might partially explain the photocatalytic degradation of the MO dye under visible light by the GOT composites, it cannot account for the photodegradation and mineralization of the colorless DP pharmaceutical, which does not absorb in the visible range. On the other hand, the visible light photocatalytic activity of the GOT composites can be most plausibly explained based on the heterogeneous electronic structure of graphene oxide, comprising a variety of electronic states that originate from different configurations of sp<sup>2</sup> and sp<sup>3</sup> hybridized carbon atoms, whose relative fractions are controlled by the degree of reduction [72]. These localized states allow GO sheets to act as sensitizers (electron donors) of TiO<sub>2</sub> upon visible light excitation [38,51]. Direct experimental evidence for



**Fig. 12.** Photocatalytic degradation of MO ( $10 \text{ mg L}^{-1}$ ) over P25 and GOT composites treated at  $200^\circ\text{C}$ , under (a) near-UV/Vis, (b) visible light irradiation. (c) Evolution of MO concentration with sample GOT-3.3-200 in cyclic (1st, 2nd and 3rd run) runs under near-UV/Vis irradiation. Catalyst load =  $0.5 \text{ g L}^{-1}$ . Curves represent the fitting of the pseudo-first order equation to the experimental data.

such a mechanism is hereby provided by the distinct quenching of the GO photoluminescence under laser excitation in the visible range upon optimal binding with  $\text{TiO}_2$  for the composites with GO content of 3.3–4.0 wt.%. In that case, electrons excited by visible light in localized  $\text{sp}^2$  states of GO with suitable energetics would be injected to the conduction band of  $\text{TiO}_2$ , where they can be readily scavenged by  $\text{O}_2$  molecules to produce reactive radicals that would attack pollutant molecules, by a process analogous to dye sensitized  $\text{TiO}_2$  photocatalysis [50].

As a first approach towards research on catalyst stability, the most active photocatalyst (GOT-3.3-200) was tested in successive photocatalytic reactions for MO degradation under near-UV/Vis irradiation. The photocatalyst was employed in three consecutive photocatalytic experiments. The experimental procedure was similar to that described in Section 2, but in this particular case, after each photocatalytic reaction, the photocatalyst was washed with water and dried in the oven at  $383 \text{ K}$  for 3 h before reused. Fig. 12c shows a marked decrease of photocatalytic activity between the first and second run, which can be explained by the presence of reaction by-products adsorbed on the photocatalyst after the first run, influencing the MO removal in the second run. Nevertheless, in the third run, the photocatalytic activity of GOT-3.3-200 remains almost unchanged with respect to the second run, indicating

catalyst stability. Even so, further studies will be required, for instance in flow reactors, to prove catalyst long term stability.

### 3.2.3. Effect of scavengers agents (EDTA/t-BuOH) in photocatalytic experiments

In order to provide more insight to the mechanism underlying the photocatalytic reaction process, a series of comparative tests were also conducted employing hole and radical trapping agents (with  $10 \text{ mM}$  of EDTA or t-BuOH, respectively) for the degradation of DP under near-UV/Vis and visible light irradiation with bare  $\text{TiO}_2$  ( $\text{TiO}_2$ -200) and one of the more active composites (GOT-3.3-200) [90].

Fig. 13a shows the results obtained with bare  $\text{TiO}_2$ -200, where the presence of t-BuOH leads to a decrease of the DP degradation. As shown in Table 2, the pseudo-first order rate constant decreases from  $16.8 \times 10^{-3}$  to  $11.1 \times 10^{-3} \text{ min}^{-1}$  in the absence and presence of t-BuOH, respectively. These results indicate that reactive species, such as hydroxyl ( $\text{HO}^\bullet$ ) and hydroperoxyl ( $\text{HOO}^\bullet$ ) radicals, participate in the photocatalytic mechanism, but they are not the major oxidation species in the process since the addition of a hole scavenger, EDTA, reduced to a much higher extent the photodegradation rate of DP ( $k = 2.1 \times 10^{-3} \text{ min}^{-1}$ , that approaches the value determined for photolysis,  $0.90 \times 10^{-3} \text{ min}^{-1}$ ). Thus,

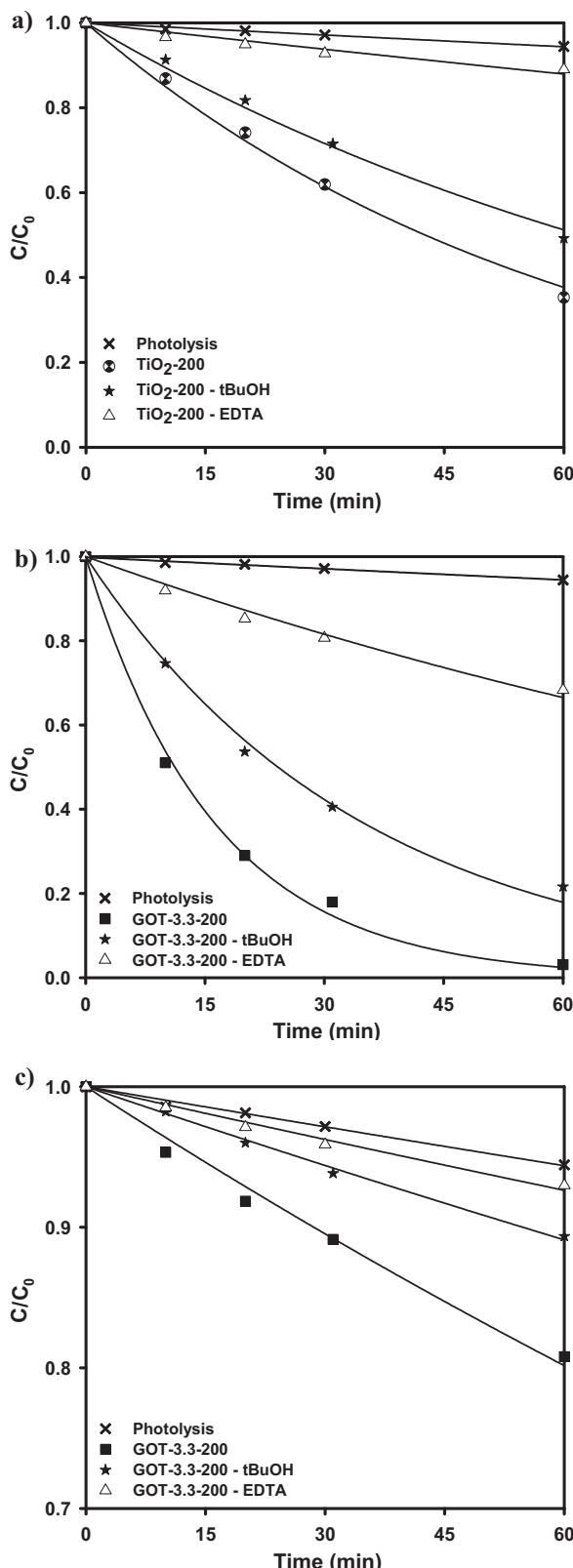


**Fig. 13.** Effect of hole/radical scavengers (EDTA/t-BuOH) on the photocatalytic degradation of DP for (a) TiO<sub>2</sub>-200 under near-UV/Vis, (b) GOT-3.3-200 under near-UV/Vis and (c) GOT-3.3-200 under visible light irradiation. Curves represent the fitting of the pseudo-first order equation to the experimental data.

photogenerated holes ( $\text{h}^+$ ) on the catalyst surface must be the major active species participating in the DP degradation process.

The same methodology was subsequently applied in DP photocatalytic experiments over GOT-3.3-200 under near-UV/Vis and visible light irradiation (Fig. 13b and c, respectively). The results showed that under near-UV/Vis irradiation the addition of t-BuOH reduces the photocatalytic degradation of DP; the pseudo-first order rate constant decreases from  $62.3 \times 10^{-3}$  to  $28.7 \times 10^{-3} \text{ min}^{-1}$  in the absence and presence of t-BuOH, respectively. However, the addition of EDTA resulted in a marked decrease of the DP photodegradation rate ( $k = 6.80 \times 10^{-3} \text{ min}^{-1}$ ), confirming that photogenerated holes were also the main reactive species in this system (ca. 88–89% decrease on the pseudo-first order rate constant for both GOT-3.3-200 and TiO<sub>2</sub>-200). Moreover, DP degradation by means of radicals is found to be considerably more effective for GOT-3.3-200 than in the case of TiO<sub>2</sub>-200 (ca. 54 and 34% decrease on the pseudo-first order rate constant for GOT-3.3-200 and TiO<sub>2</sub>-200, respectively, in the presence of t-BuOH). This behaviour could be further associated with the possibility of graphene oxide generating more reactive radicals via the reactivation of stored and transported electrons from UV irradiated TiO<sub>2</sub> that subsequently may react with adsorbed O<sub>2</sub> to form superoxide (O<sub>2</sub><sup>•-</sup>) and hydroxyl (HO<sup>•</sup>) radicals, which in turn oxidize pollutant molecules [87].

Under visible light irradiation, the radical and hole trapping experiments showed similar results (Fig. 13c). In that case, the corresponding rate constant  $k$  decreased from  $3.40 \times 10^{-3} \text{ min}^{-1}$ , in the absence of any scavenger, to  $1.90 \times 10^{-3}$  and  $1.30 \times 10^{-3} \text{ min}^{-1}$  in the presence of t-BuOH and EDTA, respectively (Table 2), showing that both radicals and holes are active species and participate on nearly equal footing in the photocatalytic oxidation reaction under visible light irradiation.

The enhanced role of radical mediated oxidation under visible compared to UV light, along with the distinct PL quenching in the GOT composites under visible laser excitation, corroborates the contribution of a sensitizing function of graphene oxide in the GOT composites. In that case, the visible light photocatalytic reaction is driven by the injection of electrons in the TiO<sub>2</sub> conduction band, followed by the fast and kinetically favoured electron transfer to dissolved O<sub>2</sub> towards the production of oxygen radicals that initiate pollutant (and/or intermediate) degradation by secondary auto-catalytic dark reactions [50].

This reinforces the action of graphene oxide as a visible light sensitizer of TiO<sub>2</sub>, which, combined with the high reactivity of GOT under UV irradiation that surpasses the P25 photocatalyst in the whole UV/Vis range, could pave the way towards the development of highly active composite photocatalysts under both UV and visible light. Further improvements of the GO-TiO<sub>2</sub> interfacial coupling could effectively circumvent titania's limitations of poor light harvesting in the visible spectral range and relatively low photocatalytic efficiency due to detrimental electron–hole recombination.

#### 4. Conclusions

Reduced graphene oxide–TiO<sub>2</sub> composites with different GO contents were prepared by using the liquid phase deposition method and subsequent post-reduction upon thermal treatment under N<sub>2</sub> at two different temperatures, 200 °C and 350 °C. The GOT composites exhibited a porous structure with high surface area, the morphology depending on the GO content and concomitant variation in the distribution of the self-assembled TiO<sub>2</sub> nanoparticles on the GO platelets. The photocatalytic efficiency of the GOT composites for the degradation of hazardous water pollutants, the DP pharmaceutical and MO azo-dye under near-UV/Vis and visible light irradiation, was found to depend markedly on the GO content

and post-calcination temperature. Almost complete degradation and significant mineralization of both pollutants was achieved within less than 60 min under near-UV/Vis irradiation for GOT composites treated at 200 °C with 3.3–4.0 wt.% GO.

SEM together with porosimetry analysis and Raman spectroscopy revealed that optimal assembly and interfacial coupling of the TiO<sub>2</sub> nanoparticles over the GO sheets is realized at these compositions. On the other hand, as-grown materials, as well as composites with higher GO content and/or reduced at higher calcination temperature (350 °C), resulted in detrimental effects on the GO-TiO<sub>2</sub> binding. The photocatalytic activity of the optimal GOT composites exceeded that of the benchmark P25 photocatalyst for both DP and MO pollutants, especially under visible light, where P25 is fairly inactive. This indicates that reduced GO-TiO<sub>2</sub> heterostructures may effectively enhance the photocatalytic activity of TiO<sub>2</sub> in the visible range without compromising the performance under UV irradiation, a major drawback of visible light active anion doped TiO<sub>2</sub> photocatalysts.

Photogenerated holes were identified as the main reactive species in DP photocatalytic degradation process for both bare TiO<sub>2</sub> and GOT composites under UV/Vis irradiation, according to photocatalytic experiments in the presence of hole (EDTA) and radical (t-BuOH) scavengers. However, an enhanced contribution of radical mediated oxidation was evidenced under visible light, which, together with the distinct quenching of the GO photoluminescence under visible and NIR laser excitation, indicate that reduced GO may also operate as a visible light sensitizer of TiO<sub>2</sub>, enabling electron transfer from GO to TiO<sub>2</sub> under visible light.

Relying on these results and the inhomogeneous variation of the size of sp<sup>2</sup> clusters and the corresponding distribution of the localized  $\pi$  and  $\pi^*$  energy states in reduced GO, it was accordingly inferred that the GO sheets upon binding with TiO<sub>2</sub> can act as electron acceptor or electron donor under UV and visible light excitation, respectively. Optimization of the GO-TiO<sub>2</sub> interface could be thus a very promising route to improve charge separation and, most importantly, to extend the photocatalytic activity of TiO<sub>2</sub> into the visible range.

## Acknowledgements

Financial support for this work was provided by the European Commission (Clean Water – Grant Agreement no. 227017), partially by projects PTDC/AAC-AMB/122312/2010 and PEst-C/EQB/LA0020/2011, financed by FEDER through COMPETE and by FCT – Fundação para a Ciência e a Tecnologia. Clean Water is a Collaborative Project co-funded by the Research DG of the European Commission within the joint RTD activities of the Environment and NMP Thematic Priorities. SMT and AMTS acknowledge financial support from SFRH/BPD/74239/2010 and POCI/N010/2006, respectively. Technical assistance by Dr. Carlos Sá and CEMUP team with SEM, AFM and XPS analysis is gratefully acknowledged.

## References

- [1] H.P. Boehm, A. Clauss, G. Fischer, U. Hofmann, *Zeitschrift für Naturforschung* 17b (1962) 150–153 (for an english translation see same author list, Proc. of the Fifth Conference on Carbon, Pergamon Press, London, 1962, p. 73).
- [2] K.S. Novoselov, A.K. Geim, S.V. Morozov, D. Jiang, Y. Zhang, S.V. Dubonos, I.V. Grigorieva, A.A. Firsov, *Science* 306 (2004) 666–669.
- [3] A.K. Geim, K.S. Novoselov, *Nature Materials* 6 (2007) 183–191.
- [4] O.V. Prezhdo, P.V. Kamat, G.C. Schatz, *The Journal of Physical Chemistry C* 115 (2011) 3195–3197.
- [5] S. Guo, S. Dong, E. Wang, *ACS Nano* 4 (2009) 547–555.
- [6] B. Seger, P.V. Kamat, *The Journal of Physical Chemistry C* 113 (2009) 7990–7995.
- [7] Y. Wang, Y. Shao, D.W. Matson, J. Li, Y. Lin, *ACS Nano* 4 (2010) 1790–1798.
- [8] G.K. Dimitrakakis, E. Tylianakis, G.E. Froudakis, *Nano Letters* 8 (2008) 3166–3170.
- [9] M. Pumera, *Energy & Environmental Science* 4 (2011) 668–674.
- [10] S. Chen, J. Zhu, X. Wu, Q. Han, X. Wang, *ACS Nano* 4 (2010) 2822–2830.
- [11] Y. Wang, Z. Shi, Y. Huang, Y. Ma, C. Wang, M. Chen, Y. Chen, *The Journal of Physical Chemistry C* 113 (2009) 13103–13107.
- [12] D.R. Dreyer, H.-P. Jia, C.W. Bielawski, *Angewandte Chemie International Edition* 49 (2010) 6813–6816.
- [13] Q. Xiang, J. Yu, M. Jaroniec, *Chemical Society Reviews* 41 (2012) 782–796.
- [14] U.I. Gaya, A.H. Abdullah, *Journal of Photochemistry and Photobiology C: Photocatalysis* 9 (2008) 1–12.
- [15] F. Méndez-Arriaga, S. Espugras, J. Giménez, *Water Research* 42 (2008) 585–594.
- [16] M.R. Hoffmann, S.T. Martin, W.Y. Choi, D.W. Bahnemann, *Chemical Reviews* 95 (1995) 69–96.
- [17] M.G. Antoniou, D.D. Dionysiou, *Catalysis Today* 124 (2007) 215–223.
- [18] M.D. Hernandez-Alonso, F. Fresno, S. Suarez, J.M. Coronado, *Energy & Environmental Science* 2 (2009) 1231–1237.
- [19] D. Dionysiou, A.P. Khodadoust, A.M. Kern, M.T. Suidan, I. Baudin, J.M. Laine, *Applied Catalysis B-Environmental* 24 (2000) 139–155.
- [20] W. Choi, *Catalysis Surveys from Asia* 10 (2006) 16–28.
- [21] A. Fujishima, X. Zhang, D.A. Tryk, *Surface Science Reports* 63 (2008) 515–582.
- [22] V. Likodimos, D. Dionysiou, P. Falaras, *Reviews in Environmental Science and Biotechnology* 9 (2010) 87–94.
- [23] A. Kubacka, M. Fernández-García, G. Colón, *Chemical Reviews* 112 (2011) 1555–1614.
- [24] L.-W. Zhang, H.-B. Fu, Y.-F. Zhu, *Advanced Functional Materials* 18 (2008) 2180–2189.
- [25] C. Chen, M. Long, H. Zeng, W. Cai, B. Zhou, J. Zhang, Y. Wu, D. Ding, D. Wu, *Journal of Molecular Catalysis A: Chemical* 314 (2009) 35–41.
- [26] C.G. Silva, J.L. Faria, *Applied Catalysis B: Environmental* 101 (2010) 81–89.
- [27] D. Li, M.B. Muller, S. Gilje, R.B. Kaner, G.G. Wallace, *Nature Nanotechnology* 3 (2008) 101–105.
- [28] S. Stankovich, D.A. Dikin, R.D. Piner, K.A. Kohlhaas, A. Kleinhammes, Y. Jia, Y. Wu, S.T. Nguyen, R.S. Ruoff, *Carbon* 45 (2007) 1558–1565.
- [29] P.V. Kamat, *The Journal of Physical Chemistry Letters* 1 (2009) 520–527.
- [30] K.P. Loh, Q. Bao, G. Eda, M. Chhowalla, *Nature Chemistry* 2 (2010) 1015–1024.
- [31] G. Williams, B. Seger, P.V. Kamat, *ACS Nano* 2 (2008) 1487–1491.
- [32] I.V. Lightcap, T.H. Kosel, P.V. Kamat, *Nano Letters* 10 (2010) 577–583.
- [33] Y. Zhang, Z.-R. Tang, X. Fu, Y.-J. Xu, *ACS Nano* 5 (2011) 7426–7435.
- [34] G. Jiang, Z. Lin, C. Chen, L. Zhu, Q. Chang, N. Wang, W. Wei, H. Tang, *Carbon* 49 (2011) 2693–2701.
- [35] F. Wang, K. Zhang, *Journal of Molecular Catalysis A: Chemical* 345 (2011) 101–107.
- [36] Y. Liang, H. Wang, H. Sanchez Casalongue, Z. Chen, H. Dai, *Nano Research* 3 (2010) 701–705.
- [37] H. Zhang, X. Lv, Y. Li, Y. Wang, J. Li, *ACS Nano* 4 (2009) 380–386.
- [38] C. Chen, W. Cai, M. Long, B. Zhou, Y. Wu, D. Wu, Y. Feng, *ACS Nano* 4 (2010) 6425–6432.
- [39] T.N. Lambert, C.A. Chavez, B. Hernandez-Sánchez, P. Lu, N.S. Bell, A. Ambrosini, T. Friedman, T.J. Boyle, D.R. Wheeler, D.L. Huber, *The Journal of Physical Chemistry C* 113 (2009) 19812–19823.
- [40] X.-Y. Zhang, H.-P. Li, X.-L. Cui, Y. Lin, *Journal of Materials Chemistry* 20 (2010) 2801–2806.
- [41] Y. Zhang, Z.-R. Tang, X. Fu, Y.-J. Xu, *ACS Nano* 4 (2010) 7303–7314.
- [42] J. Du, X. Lai, N. Yang, J. Zhai, D. Kisailus, F. Su, D. Wang, L. Jiang, *ACS Nano* 5 (2010) 590–596.
- [43] K. Zhou, Y. Zhu, X. Yang, X. Jiang, C. Li, *New Journal of Chemistry* 35 (2011) 353–359.
- [44] W. Fan, Q. Lai, Q. Zhang, Y. Wang, *The Journal of Physical Chemistry C* 115 (2011) 10694–10701.
- [45] J. Liu, L. Liu, H. Bai, Y. Wang, D.D. Sun, *Applied Catalysis B: Environmental* 106 (2011) 76–82.
- [46] Q. Xiang, J. Yu, M. Jaroniec, *Nanoscale* 3 (2011) 3670–3678.
- [47] J. Zhang, Z. Xiong, X.S. Zhao, *Journal of Materials Chemistry* 21 (2011) 3634–3640.
- [48] Y. Wen, H. Ding, Y. Shan, *Nanoscale* 3 (2011) 4411–4417.
- [49] S. Morales-Torres, L.M. Pastrana-Martínez, J.L. Figueiredo, J.L. Faria, A.M.T. Silva, *Environmental Science and Pollution Research*, <http://dx.doi.org/10.1007/s11356-012-0939-4>, in press.
- [50] D. Chatterjee, S. Dasgupta, *Journal of Photochemistry and Photobiology C: Photocatalysis* 6 (2005) 186–205.
- [51] A. Du, Y.H. Ng, N.J. Bell, Z. Zhu, R. Amal, S.C. Smith, *The Journal of Physical Chemistry Letters* 2 (2011) 894–899.
- [52] L.M. Pastrana-Martínez, J.L. Faria, J.M. Doña-Rodríguez, C. Fernández-Rodríguez, A.M.T. Silva, *Applied Catalysis B: Environmental* 113–114 (2012) 221–227.
- [53] C.A. Kinney, E.T. Furlong, S.L. Werner, J.D. Cahill, *Environmental Toxicology and Chemistry* 25 (2006) 317–326.
- [54] A. Mittal, A. Malviya, D. Kaur, J. Mittal, L. Kurup, *Journal of Hazardous Materials* 148 (2007) 229–240.
- [55] W.S. Hummers, R.E. Offeman, *Journal of the American Chemical Society* 80 (1958), 1339–1339.
- [56] S. Brunauer, P.H. Emmett, E. Teller, *Journal of the American Chemical Society* 60 (1938) 309–319.
- [57] F. Stoeckli, in: J.W. Patrick (Ed.), *Porosity in Carbons: Characterization and Applications*, Edward Arnold, London, 1995, pp. 66–97.
- [58] E.P. Barrett, L.G. Joyner, P.P. Halenda, *Journal of the American Chemical Society* 73 (1951) 373–380.

[59] M.J. McAllister, J.-L. Li, D.H. Adamson, H.C. Schniepp, A.A. Abdala, J. Liu, M. Herrera-Alonso, D.L. Milius, R. Car, R.K. Prud'homme, I.A. Aksay, *Chemistry of Materials* 19 (2007) 4396–4404.

[60] J.I. Paredes, S. Villar-Rodil, P. Solís-Fernandez, A. Martínez-Alonso, J.M.D. Tascon, *Langmuir* 25 (2009) 5957–5968.

[61] H. Varela-Rizo, I. Rodriguez-Pastor, C. Merino, I. Martin-Gullon, *Carbon* 48 (2010) 3640–3643.

[62] S. Fujii, T. Enoki, *Journal of the American Chemical Society* 132 (2010) 10034–10041.

[63] W. Peng, Z. Wang, N. Yoshizawa, H. Hatori, T. Hirotsu, K. Miyazawa, *Journal of Materials Chemistry* 20 (2010) 2424–2431.

[64] S. Brunauer, L.S. Deming, W.E. Deming, E. Teller, *Journal of the American Chemical Society* 62 (1940) 1723–1732.

[65] O. Akhavan, E. Ghaderi, *The Journal of Physical Chemistry C* 113 (2009) 20214–20220.

[66] S. Shammugam, A. Gabashvili, D.S. Jacob, J.C. Yu, A. Gedanken, *Chemistry of Materials* 18 (2006) 2275–2282.

[67] L. Zhang, P. Liu, Z. Su, *Journal of Molecular Catalysis A: Chemical* 248 (2006) 189–197.

[68] S. Sakthivel, H. Kisch, *Angewandte Chemie International Edition* 42 (2003) 4908–4911.

[69] A.C. Ferrari, J. Robertson, *Philosophical Transactions of the Royal Society of London. Series A: Mathematical, Physical and Engineering Sciences* 362 (2004) 2477–2512.

[70] M.S. Dresselhaus, A. Jorio, M. Hofmann, G. Dresselhaus, R. Saito, *Nano Letters* 10 (2010) 751–758.

[71] Z. Luo, P.M. Vora, E.J. Mele, A.T.C. Johnson, J.M. Kikkawa, *Applied Physics Letters* 94 (2009) 111909.

[72] G. Eda, Y.-Y. Lin, C. Mattevi, H. Yamaguchi, H.-A. Chen, I.S. Chen, C.-W. Chen, M. Chhowalla, *Advanced Materials* 22 (2010) 505–509.

[73] T.V. Cuong, V.H. Pham, Q.T. Tran, S.H. Hahn, J.S. Chung, E.W. Shin, E.J. Kim, *Materials Letters* 64 (2010) 399–401.

[74] K.N. Kudin, B. Ozbas, H.C. Schniepp, R.K. Prud'homme, I.A. Aksay, R. Car, *Nano Letters* 8 (2007) 36–41.

[75] M.A. Pimenta, G. Dresselhaus, M.S. Dresselhaus, L.G. Cancado, A. Jorio, R. Saito, *Physical Chemistry Chemical Physics* 9 (2007) 1276–1290.

[76] T. Gokus, R.R. Nair, A. Bonetti, M. Bohmler, A. Lombardo, K.S. Novoselov, A.K. Geim, A.C. Ferrari, A. Hartschuh, *ACS Nano* 3 (2009) 3963–3968.

[77] M.M. Lucchese, F. Stavale, E.H.M. Ferreira, C. Vilani, M.V.O. Moutinho, R.B. Capaz, C.A. Achete, A. Jorio, *Carbon* 48 (2010) 1592–1597.

[78] D. Yang, A. Velamakanni, G. Bozoklu, S. Park, M. Stoller, R.D. Piner, S. Stankovich, I. Jung, D.A. Field, C.A. Ventrice Jr., R.S. Ruoff, *Carbon* 47 (2009) 145–152.

[79] C. Mattevi, G. Eda, S. Agnoli, S. Miller, K.A. Mkhoyan, O. Celik, D. Mastrogiovanni, G. Granozzi, E. Garfunkel, M. Chhowalla, *Advanced Functional Materials* 19 (2009) 2577–2583.

[80] D. Zhan, Z. Ni, W. Chen, L. Sun, Z. Luo, L. Lai, T. Yu, A.T.S. Wee, Z. Shen, *Carbon* 49 (2011) 1362–1366.

[81] V. Swamy, A. Kuznetsov, L.S. Dubrovinsky, R.A. Caruso, D.G. Shchukin, B.C. Muddle, *Physical Review B* 71 (2005) 184302.

[82] V. Likodimos, T. Stergiopoulos, P. Falaras, J. Kunze, P. Schmuki, *The Journal of Physical Chemistry C* 112 (2008) 12687–12696.

[83] C. Casiraghi, A.C. Ferrari, J. Robertson, *Physical Review B* 72 (2005) 085401.

[84] I. Mora-Seró, V. Likodimos, S. Giménez, E. Martínez-Ferrero, J. Albero, E. Palomares, A.G. Kontos, P. Falaras, J. Bisquert, *The Journal of Physical Chemistry C* 114 (2010) 6755–6761.

[85] C. Han, M. Pelaez, V. Likodimos, A.G. Kontos, P. Falaras, K. O'Shea, D.D. Dionysiou, *Applied Catalysis B: Environmental* 107 (2011) 77–87.

[86] T.-D. Nguyen-Phan, V.H. Pham, E.W. Shin, H.-D. Pham, S. Kim, J.S. Chung, E.J. Kim, S.H. Hur, *Chemical Engineering Journal* 170 (2011) 226–232.

[87] J. Liu, H. Bai, Y. Wang, Z. Liu, X. Zhang, D.D. Sun, *Advanced Functional Materials* 20 (2010) 4175–4181.

[88] R. Czerw, B. Foley, D. Tekleab, A. Rubio, P.M. Ajayan, D.L. Carroll, *Physical Review B* 66 (2002) 033408.

[89] X. Wang, L. Zhi, K. Mullen, *Nano Letters* 8 (2007) 323–327.

[90] M. Yin, Z. Li, J. Kou, Z. Zou, *Environmental Science & Technology* 43 (2009) 8361–8366.